# Probing 3D magnetic fields using starlight polarization and grain alignment theory

BAO TRUONG. 1,2 THIEM HOANG. 1,2

<sup>1</sup>Korea Astronomy and Space Science Institute, Daejeon 34055, Republic of Korea <sup>2</sup>Department of Astronomy and Space Science, University of Science and Technology, 217 Gajeong-ro, Yuseong-qu, Daejeon, 34113, Republic of Korea

### ABSTRACT

Polarization of starlight induced by dust grains aligned with the magnetic field (hereafter B-field) is widely used to measure the two-dimensional B-fields projected onto the plane-of-sky. Here, we introduce a new method to infer three-dimensional B-fields using starlight polarization. The B-field's inclination angle or line-of-sight (LOS) component of B-fields is constrained by the starlight polarization efficiency from observations and the alignment degree provided by the magnetically enhanced radiative torque (MRAT) alignment theory. We first perform synthetic observation of starlight polarization of magnetohydrodynamic (MHD) simulations of a filamentary cloud. We then test the new technique with our updated POLARIS code and find that the B-field's inclination angles can be precisely determined by the starlight polarization efficiency from synthetic observations. Regardless of grain magnetic properties, the technique can provide an accurate constraint on B-field's inclination angles in lowdensity regions  $N_{\rm H} < 5 \times 10^{21}~{\rm cm}^{-2}$  (or visual extinction  $A_V < 3$ ) using optical polarization, whereas the technique can infer further to high-density regions  $N_{\rm H}\sim 5\times 10^{22}~{\rm cm}^{-2}$  (or  $A_V\sim 30$ ) using near-infrared polarization. Our new technique opens the full potential of tracing 3D B-fields and constraining dust properties and grain alignment physics on multiple scales of the diffuse interstellar medium and star-forming regions using multi-wavelength starlight polarization observations.

### 1. INTRODUCTION

Magnetic fields (B-fields) are thought to play an important role in the evolution of the interstellar medium (ISM) and the formation of young stars and planets (Crutcher 2010). Interstellar magnetic field is first recognized through the discovery of the polarization of distant starlight (Hall 1949; Hiltner 1949). Subsequently, starlight polarization is widely used to trace the largescale B-fields in the diffuse ISM (Serkowski et al. 1975; Heiles 2000) and molecular clouds (Goodman et al. 1990. 1995) and dense cores (Kandori et al. 2020b). Starlight polarization angles could be used to measure  $B_{POS}$ (Chapman et al. 2011) using the Davis-Chandrasekhar-Fermi (DCF, Davis 1951; Chandrasekhar & Fermi 1953) technique.

The degree of starlight polarization encodes unique information on fundamental dust properties (grain size, shape, and composition), the B-field properties (inclination angle and tangling), and grain alignment effi-

baotruong@kasi.re.kr thiemhoang@kasi.re.kr and is highly ordered. The comprehensive starlight polarization survey for 364 stars by Serkowski et al. (1975) showed the maximum polarization efficiency of  $(P_V/E(B-V))_{\text{max}} \approx$ 9%/mag. However, the latest studies by Panopoulou et al. (2019) using R-band RoboPol toward a sample of 22 stars that have the highest polarization degree of thermal dust emission observed by Planck of  $P_{353\text{GHz}} \approx 20\%$  found a higher maximum polarization efficiency of  $P_V/E(B-V) \ge 13\%/\text{mag}$  (see Hensley & Draine 2021 for more details). Recently, several sur-

veys of interstellar starlight polarization are available

(Clemens et al. 2016, 2020; Versteeg et al. 2023), which provide crucial constraints on interstellar magnetic field

ciency with B-fields (Lee & Draine 1985). Therefore, the starlight polarization degree would provide the B-

field's inclination angle and the tangling (randomness)

when the grain alignment and dust properties are well

constrained Jones (1989); Jones et al. (1992). Using the

observed polarization degree of silicate feature at 9.7  $\mu$ m,

Lee & Draine (1985) first suggested that the magnetic

fields along the LOS toward the Backlin-Neugebauer

(BN) object are inclined by an angle  $\sin^2 \gamma_{\rm max} < 0.5$ 

and dust. Panopoulou et al. (2019) suggested the combination of starlight polarization with star distance from Gaia to reconstruct the variation of the plane of the sky (POS) component of magnetic fields along the LOS (2D B-field tomography). The degree of starlight polarization per extinction,  $P/A_{\rm V}$  (aka polarization efficiency), is also used to constrain the magnetic field inclination angle (Angarita et al. 2023). The practice is done as follows. By observing many stars from a sky region, one can measure the polarization efficiency,  $P/A_{\rm V}$ , for all these stars. The upper bound of the line  $P/A_{\rm V}$  vs.  $A_{\rm V}$ corresponds to the optimal conditions of the starlight polarization, including perfect grain alignment and B lying in the POS. The sightlines with lower  $P/A_{\rm V}$  are interpreted as having an inclined magnetic field. However, this approach assumes that grain alignment is perfect and attributes all the depolarization to the B-field inclination angle (Angarita et al. 2023; Doi et al. 2024). To unleash the full potential of starlight polarization in probing dust properties and B-fields, a detailed study on the effect of grain alignment and B-fields on the starlight polarization must be quantified to accurately infer the inclination angle using the starlight polarization efficiency.

Grain alignment physics is a long-standing problem in astrophysics (Davis & Greenstein 1951; Jones & Spitzer 1967; Purcell 1979). The leading theory of grain alignment is now based on the Radiative Torques (RATs), initially studied by Dolginov & Mitrofanov (1976) and numerically quantified by Draine & Weingartner (1996, 1997). The quantitative theory of grain alignment based on RATs is developed in Lazarian & Hoang (2007); Hoang & Lazarian (2008, 2014). The successful development of the unified theory of grain alignment by the joint effect of magnetic relaxation and RATs by Hoang et al. (2016) allows us to predict the alignment degree as a function of the local properties and dust properties. Hoang & Truong (2024) first incorporated grain alignment physics into the thermal dust polarization model and introduced an improved technique to constrain 3D B-fields using the observed polarization data. The testing using synthetic polarization of MHD simulations revealed a successful recovery of the B-fields. In this follow-up paper, for the first time, we aim to extend the technique to starlight polarization using a similar approach in Hoang & Truong (2024) by using synthetic observations of starlight polarization using MHD simulations for the turbulent magnetized filament using the modern MRAT alignment theory.

The structure of this paper is as follows. In Section 2 we introduce a physical model of starlight polarization based on the MRAT mechanism and present a new

method for constraining 3D B-fields using starlight polarization. In Section 3, we will test the starlight polarization model using synthetic polarization observations of MHD simulations. In Section 4 we will present our numerical results, compare them with the polarization from the analytical model, and apply our method for inferring the inclination angles using the synthetic starlight polarization. An extended discussion of our results and implications are presented in Section 5, and a summary is shown in Section 6.

### 2. METHODS

# 2.1. Starlight Polarization Model

### 2.1.1. Uniform magnetic field

Let  $\hat{\mathbf{z}}$  be the line of sight, and the plane of the sky is  $\hat{\mathbf{x}}\hat{\mathbf{y}}$  (see Figure 1). The regular magnetic field  $\mathbf{B}_0$  is assumed to make an angle  $\gamma$  with the LOS, and the fluctuations of the local magnetic field along the LOS are first ignored for simplicity. Let  $C_x, C_y$  be the extinction cross-section of a grain for the electric fields along  $\hat{\mathbf{x}}$  and  $\hat{\mathbf{y}}$ , respectively. The difference in  $C_x$  and  $C_y$  induced by partially aligned grains is given by (Lee & Draine 1985; Hoang & Truong 2024)

$$C_y - C_x = C_{\text{pol}} f_{\text{align}} \sin^2 \gamma, \tag{1}$$

where  $C_{\text{pol}}$  is the polarization cross-section of the grain, and  $f_{\text{align}}$  is the degree of grain alignment with the magnetic field which will be determined in the next section.

The intensity of transmission light from stars with the incident electric field along  $\hat{\mathbf{x}}$  and  $\hat{\mathbf{y}}$  is given by, respectively

$$I_x(\mathbf{E}||\hat{\mathbf{x}}) = I_{0x}e^{-\tau_x}, \quad I_y(\mathbf{E}||\hat{\mathbf{y}}) = I_{0y}e^{-\tau_y},$$
 (2)

where  $I_{0x} = I_{0y} = I_0/2$  with  $I_0$  is the total intensity of unpolarized incident starlight, and  $\tau_x, \tau_y$  are the optical depth for the incident electric field along the  $\hat{\mathbf{x}}$  and  $\hat{\mathbf{y}}$  axes.

The polarization degree of transmission starlight is defined by

$$P_{\text{ext}} = \frac{I_y(\mathbf{E}||\hat{\mathbf{y}}) - I_x(\mathbf{E}||\hat{\mathbf{x}})}{I_y(\mathbf{E}||\hat{\mathbf{y}}) + I_x(\mathbf{E}||\hat{\mathbf{x}})} = \frac{e^{-\tau_x} - e^{-\tau_y}}{e^{-\tau_x} + e^{-\tau_y}} = \tanh\left(\frac{\tau_y - \tau_x}{2}\right) 3$$

where  $\tau_{\text{pol}} = \tau_x - \tau_y$  is the polarized optical depth.

For the case of small polarized extinction with  $\tau_{\rm pol} \ll 1$ , one obtains

$$P_{\text{ext}} \approx \frac{\tau_y - \tau_x}{2 + \tau_y + \tau_x} \approx \left(\frac{\tau_y - \tau_x}{2}\right).$$
 (4)

For the case of large polarized extinction with  $\tau_{\rm pol} \gg 1$ , one has  $\tanh(\tau_{\rm pol}) \to 1$ , so that the polarization degree by extinction achieves the maximum level given by  $P_{\rm ext} = 1$ .

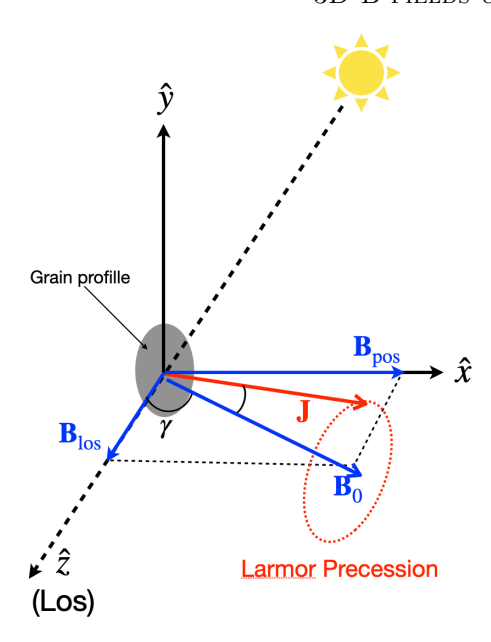


Figure 1. Illustration of the effect of grain alignment, the mean magnetic field  $\boldsymbol{B}$ , and the line of sight  $\hat{\mathbf{z}}$  from Hoang & Truong (2024). The mean B-field lies in the plane  $\hat{\mathbf{x}}\hat{\mathbf{z}}$  and makes an angle  $\gamma$  with the line of sight. The grain axis of maximum inertia is assumed to be aligned with  $\boldsymbol{B}$ . The difference in the cross-sections along  $\hat{\mathbf{x}}$  and  $\hat{\mathbf{y}}$  induces the polarization of transmission starlight.

We first consider the case of a uniform environment where dust properties and grain alignment do not change significantly along the LOS. Using the relationship between  $\tau_y - \tau_x$  and the grain alignment model in Hoang & Truong (2024), one obtains the polarization of starlight by extinction for the case of small polarized extinction (Equation 4):

$$P_{\rm ext}(\lambda) = N_{\rm H} \sin^2 \gamma \int_{a_{\rm min}}^{a_{\rm max}} da n_d(a) C_{\rm pol}(a, \lambda) f_{\rm align}(a) (5)$$

where  $N_{\rm H}$  is the column density of hydrogen nucleon along the LOS,  $n_d(a)$  is the grain size distribution with the lower and upper cutoff of  $a_{\rm min}$  to  $a_{\rm max}$ .

# 2.1.2. Polarization Efficiency

The degree of starlight polarization per hydrogen atom (i.e., polarization efficiency) can also be written as

$$\frac{P_{\rm ext}(\lambda)}{N_{\rm H}} = \sin^2 \gamma \times \sigma_{\rm pol, align}(\lambda), \tag{6}$$

where

$$\sigma_{\rm pol,align}(\lambda) = \int_{a_{\rm min}}^{a_{\rm max}} dan_d(a) C_{\rm pol}(a, \lambda) f_{\rm align}(a),$$
 (7)

is the polarization coefficient of aligned grains at the wavelength  $\lambda$  (in units of cm<sup>2</sup> H<sup>-1</sup>).

The fractional polarization (i.e., the ratio of observed polarization to extinction) is defined by

$$\frac{P_{\text{ext}}(\lambda)}{\tau_{\lambda}} = \frac{\sigma_{\text{pol,align}}(\lambda)\sin^{2}\gamma}{\sigma_{\text{ext}}(\lambda)},$$
 (8)

where  $\tau_{\lambda} = 1.086 N_{\rm H} \sigma_{\rm ext}(\lambda)$  is the optical depth, and  $\sigma_{\rm ext}(\lambda)$  is the extinction coefficient.

# 2.1.3. Effect of magnetic field fluctuations

Magnetic fluctuations with respect to the mean B-field have a significant influence on the observed starlight polarization degree (Lee & Draine 1985). Let  $\delta\theta$  be the angle between the local magnetic field and the mean B-field. Assuming that the turbulent field component is perpendicular to the mean field (i.e., Alfvenic turbulence),  $B_0$ , the local magnetic field reads

$$\boldsymbol{B} = \boldsymbol{B}_0 + \delta \boldsymbol{B}_\perp, \tag{9}$$

where we disregarded the compressive modes of turbulence of  $\delta B_{\parallel}$ .

For this case, the polarization cross-section (Equation 1) becomes (Lee & Draine 1985)

$$C_y - C_x = C_{\text{pol}} f_{\text{align}} \sin^2 \gamma F_{\text{turb}},$$
 (10)

where

$$F_{\text{turb}} = \frac{1}{2} 3 \langle \cos^2(\delta \theta) \rangle - 1. \tag{11}$$

For small fluctuations of  $\delta\theta$  < 1, one can make the approximation (Hoang & Truong 2024)

$$F_{\text{turb}} = 1 - 1.5 \langle \sin^2(\Delta\theta) \rangle \approx 1 - 1.5 (\delta\theta)^2,$$
 (12)

where  $\delta\theta$  is the inclination angle dispersion.

One obtains that the increase in the angle dispersion  $\delta\theta$  reduces the value of  $F_{\rm turb}$ , which then decreases the starlight polarization efficiency. Therefore, when taking into account the LOS fluctuations, one needs to incorporate the factor  $F_{\rm turb} \propto 1 - (\delta\theta)^2$ . In the case of isotropic turbulence, the polarization angle dispersion  $\delta\phi$  corresponds to  $\delta\theta$ , and the starlight polarization degree is then inversely proportional to  $(\delta\phi)^2$  (see also the interpretation in Hoang & Truong 2024).

The polarization efficiency with magnetic turbulence is now given by

$$\frac{P_{\rm ext}(\lambda)}{N_{\rm H}} = \sin^2 \gamma \times \sigma_{\rm pol,align}(\lambda) \times F_{\rm turb}.$$
 (13)

# 2.1.4. Starlight Polarization Integral

Following Draine & Hensley (2021) (hereafter DH21), we define the starlight polarization integral as

$$\Pi = \frac{\int_{\lambda} P_{\text{ext}}(\lambda) d\lambda}{N_{\text{H}}},\tag{14}$$

which integrates over the starlight polarization spectrum.

Using the polarization extinction from Equation 13 for the above equation, one can write

$$\begin{split} \frac{\Pi}{\sin^2 \gamma F_{\text{turb}}} &= \frac{\int_{\lambda} P_{\text{ext}}(\lambda) d\lambda}{N_{\text{H}} \sin^2 \gamma F_{\text{turb}}} \\ &= \int_{a_{\text{amin}}}^{a_{\text{max}}} da n_d(a) \left[ \int_{\lambda} C_{\text{pol}}(a, \lambda) d\lambda \right] f_{\text{align}}(a) \\ &= \int_{a_{\text{amin}}}^{a_{\text{max}}} da n_d(a) \left[ \frac{\int C_{\text{pol}}(a, \lambda) d\lambda}{V_{\text{gr}}(a)} \right] V_{gr}(a) f_{\text{align}}(a) \\ &= \int_{a_{\text{amin}}}^{a_{\text{max}}} da n_d(a) \Phi(a) V_{\text{gr}}(a) f_{\text{align}}(a), \end{split} \tag{15}$$

where

$$\Phi(a) = \frac{\int_{\lambda} C_{\text{pol}}(a,\lambda) d\lambda}{V_{ar}(a)} = \frac{3}{4\pi} \int \frac{Q_{\text{pol}}(a,\lambda)}{a} d\lambda, (16)$$

is the dimensionless starlight polarization efficiency integral and  $V_{\rm gr}(a)=(4\pi/3)a^3$  is the grain volume. The starlight polarization efficiency integral depends on both grain sizes and grain elongation (Draine & Hensley 2021).

# 2.2. Grain alignment from the MRAT theory 2.2.1. Minimum size for grain alignment

The key parameter of the RAT alignment theory is the minimum grain size required for grain alignment, denoted by  $a_{\text{align}}$ , which is given by (Hoang et al. 2021):

$$a_{\text{align}} = \left(\frac{1.2n_{\text{H}}T_{\text{gas}}}{\gamma_{\text{rad}}u_{\text{rad}}\bar{\lambda}^{-2}}\right)^{2/7} \left(\frac{15m_{\text{H}}k^{2}}{4\rho}\right)^{1/7} (1 + F_{\text{IR}})^{2/7}$$

$$\simeq 0.055\hat{\rho}^{-1/7} \left(\frac{\gamma_{-1}U}{n_{3}T_{\text{gas},1}}\right)^{-2/7}$$

$$\times \left(\frac{\bar{\lambda}}{1.2\,\mu\text{m}}\right)^{4/7} (1 + F_{\text{IR}})^{2/7} \,\mu\text{m}, \tag{17}$$

where  $\hat{\rho} = \rho/(3\,\mathrm{g\,cm^{-3}})$  is the normalized mass density of grain material,  $T_{\mathrm{gas},1} = T_{\mathrm{gas}}/10\,\mathrm{K}$  is the normalized gas temperature,  $n_3 = n_{\mathrm{H}}/(10^3\,\mathrm{cm^{-3}})$  is the normalized gas density,  $\gamma_{-1} = \gamma_{\mathrm{rad}}/0.1$  is the normalized anisotropy degree of radiation,  $\bar{\lambda}$  is the mean wavelength of the radiation field and  $U = u_{\mathrm{rad}}/u_{\mathrm{ISRF}}$  is the strength of radiation field with the energy density  $u_{\mathrm{rad}}$  over the energy density of the interstellar radiation field (ISRF) in the solar neighborhood with  $u_{\mathrm{ISRF}} = 8.6 \times 10^{-13}\,\mathrm{erg\,cm^{-3}}$  (Mathis et al. 1983).  $F_{\mathrm{IR}}$  is a dimensionless parameter that describes the grain rotational damping by infrared emission, which can be negligible in the ISM and dense clouds as  $F_{\mathrm{IR}} \ll 1$ .

# 2.2.2. Grain Alignment Degree and Alignment Function

The alignment efficiency for an ensemble of grains having a given size a is described by the Rayleigh reduction factor, R (see Greenberg 1968), which characterizes the average alignment degree of the grain axis of major inertia with the ambient magnetic field. From the modern theory of grain alignment based on RATs, the Rayleigh reduction factor is parameterized by the fractions of grains aligned at low-J and high-J attractors,

$$R = f_{\text{high-J}} Q_X^{\text{high-J}} + (1 - f_{\text{high-J}}) Q_X^{\text{low-J}}. \quad (18)$$

Numerical simulations in Hoang & Lazarian (2016a) show that if the RAT alignment has a high-J attractor point, then, grains can be perfectly aligned when they are spun up to suprathermal rotation with  $Q_X^{\mathrm{high-J}}=1$ . Meanwhile, grains at low-J attractors rotating subthermally by gas collision have smaller alignment efficiency with  $Q_X^{\mathrm{low-J}}\sim 0.3$  (Hoang & Lazarian 2016a,b)

Within the MRAT mechanism, the fraction  $f_{\text{high-J}}$  is determined by both RATs, magnetic relaxation, and gas randomization, which is approximately given by the function

$$f_{\text{high-J}} = f(\delta_{\text{mag}}),$$
 (19)

and  $\delta_{\text{mag}}$  is the magnetic relaxation strength which measures the relative strength of the magnetic relaxation to gas randomization. For grains without iron inclusions (i.e., ordinary paramagnetic material, a.k.a, PM), high-J attractors are only present for a limited range of the radiation direction that depends on the grain shape (Hoang & Lazarian 2016a).

For superparamagnetic (SPM) grains with embedded iron inclusions, the magnetic relaxation strength is enhanced and calculated as

$$\delta_{\text{mag}} = \frac{\tau_{\text{gas}}}{\tau_{\text{mag,sp}}}$$

$$= 5.6a_{-5}^{-1} \frac{N_{\text{cl}}\phi_{\text{sp},-2}\hat{p}^2 B_2^2}{\hat{\rho}n_3 T_{\text{gas},1}^{1/2}} \frac{k_{\text{sp}}(\Omega)}{T_{\text{d},1}}, \qquad (20)$$

where  $N_{\rm cl}$  and  $\phi_{\rm sp,-2} = \phi_{\rm sp}/10^{-2}$  are the number of iron inclusions and the volume filling factor,  $B_2 = B/10^2 \mu G$  is the normalized magnetic field strength and  $T_{\rm d,1} = T_{\rm d}/10\,\rm K$  is the normalized dust temperature. The relaxation strength is higher if SPM grains have an enhanced magnetic susceptibility by including higher levels of iron clusters (Lazarian & Hoang 2008; Hoang & Lazarian 2016a).

Detailed calculations of Hoang & Lazarian (2016a) shows the increase of  $f_{\text{high-J}}$  with  $\delta_{\text{mag}}$ , which can be

parameterized by (Giang et al. 2023):

$$f_{\text{high-J}}(\delta_{\text{mag}}) = \begin{cases} 0.25 & \text{for } \delta_{\text{mag}} < 1\\ 0.5 & \text{for } 1 \le \delta_{\text{mag}} \le 10\\ 1 & \text{for } \delta_{\text{mag}} > 10 \end{cases}$$
 (21)

From numerical calculations in Hoang & Lazarian (2016a) using the MRAT alignment theory, grains smaller than the critical size  $a_{\rm align}$  are weakly aligned only by paramagnetic relaxation (also Hoang & Lazarian 2016b), and grains much larger than  $a_{\rm align}$  have an alignment degree described by R. Moreover, the alignment degree increases smoothly with the grain size across  $a = a_{\rm align}$ . Therefore, we can describe the degree of grain alignment as a function of the grain size (i.e., alignment function) by multiplying R with an exponential function (Lee et al. 2020):

$$f_{\text{align}}(a) = R \times \left[1 - \exp\left(-\left(\frac{0.5a}{a_{\text{align}}}\right)^3\right)\right], \quad (22)$$

which implies that  $f_{\text{align}}$  approaches R for  $a \gg a_{\text{align}}$  and is negligible for  $a \ll a_{\text{align}}$ .

For a given grain size distribution and magnetic properties, using  $a_{\rm align}$  from the RAT theory,  $\delta_{\rm mag}$  and R, one can calculate the alignment function  $f_{\rm align}(a)$  as shown in Equation 22. Figure 2 shows an example of the analytical calculation of the grain alignment function  $f_{\rm align}$  for SPM grains with  $\phi_{\rm sp}=10^{-2}$  (i.e., only 3% of iron abundance in the form of iron clusters) and  $N_{\rm cl}=1,10$  and 100, assuming the minimum alignment size  $a_{\rm align}=0.015\,\mu{\rm m},\ T_{\rm gas}=T_{\rm d}=10$  K,  $n_{\rm H}=10^3$  cm<sup>-3</sup> and  $B=10^2\,\mu{\rm G}.$  Small grains  $a< a_{\rm align}$  are weakly aligned with B-fields with a very low alignment degree  $f_{\rm align}(a)<0.1$ , while large grains of  $a>a_{\rm align}$  are efficiently aligned by the MRAT mechanism, and can achieve perfect alignment of  $f_{\rm align}(a)=1$  as  $N_{\rm cl}>100$  (Hoang & Lazarian 2016a; Giang et al. 2023).

We have updated the POLARIS with this alignment function  $f_{\rm align}(a)$  and compared the polarization results with the piece-wise function R originally implemented in POLARIS (Reissl et al. 2016; Giang et al. 2023). We found the exponential function in  $f_{\rm align}(a)$  mostly affects starlight polarization in optical-UV which are dominated by aligned grains of  $a \sim a_{\rm align}$ , but not important for starlight polarization in NIR or polarized thermal dust emission at far-IR/submm which are dominated by large grains of  $a > a_{\rm align}$ . Therefore, the previous results on far-IR/submm polarization using POLARIS remain valid.

# 2.3. Inferring the inclination angle of the mean magnetic fields

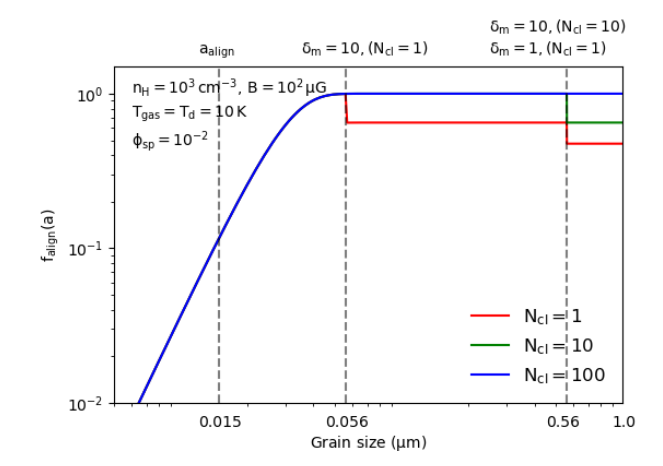


Figure 2. The analytical calculation of the alignment degree of SPM grains with  $N_{\rm cl}=1-100$  as an exponential form in Equation 22 over the grain size with  $a_{\rm align}=0.015\,\mu{\rm m}$ . The alignemnt degree increases with the grain size and large grains  $a>a_{\rm align}$  can achieve perfect magnetic alignment for  $N_{\rm cl}\sim 100$  by the MRAT mechanism.

#### 2.3.1. Using Polarization Efficiency

To infer the inclination angle of the mean magnetic field wrt to the LOS from starlight polarization observed at a wavelength  $\lambda$ , we use the equation (13):

$$\frac{P_{\rm ext}(\lambda)}{N_{\rm H}} = \sin^2 \gamma F_{\rm turb} \times \sigma_{\rm pol, align}(\lambda). \tag{23}$$

The maximum polarization efficiency occurs for the magnetic field perpendicular to the LOS (i.e.,  $\sin^2 \gamma = 1$ ), and perfect grain alignment of all grain sizes. This corresponds to the intrinsic polarization efficiency

$$\frac{P_{\rm ext,i}(\lambda)}{N_{\rm H}} = \int_{a_{\rm pol,i}}^{a_{\rm max}} dan_d(a) C_{\rm pol}(a,\lambda) = \sigma_{\rm pol,i}(\lambda), (24)$$

where  $\sigma_{\text{pol},i}(\lambda)$  is the intrinsic polarization coefficient for all grain sizes perfectly aligned with magnetic fields with  $f_{\text{align}}(a) = 1$ .

Here, we introduce the fraction of the polarization coefficient  $f_{\text{pol}}(\lambda)$  as

$$f_{\rm pol}(\lambda) = \frac{\sigma_{\rm pol, align}(\lambda)}{\sigma_{\rm pol, i}(\lambda)}.$$
 (25)

Therefore, the observed polarization efficiency (Eq. 23) can be rewritten as

$$\frac{P_{\rm ext}(\lambda)}{N_{\rm H}} = \frac{P_{\rm ext,i}(\lambda)}{N_{\rm H}} \times f_{\rm pol}(\lambda) F_{\rm turb} \sin^2 \gamma. \tag{26}$$

Thus, one can infer the inclination angle from the observed starlight polarization at the wavelength  $\lambda$  as

$$\sin^2 \gamma = \frac{1}{f_{\text{pol}}(\lambda) F_{\text{turb}}} \frac{(P_{\text{ext}}/N_{\text{H}})_{\text{obs}}}{(P_{\text{ext,i}}/N_{\text{H}})}.$$
 (27)

### 2.3.2. Using Starlight Polarization Integral

From the starlight polarization integral described in Equation 15, we also obtain the inclination angles of the mean fields as

$$\sin^2 \gamma = \frac{\Pi}{F_{\text{turb}} \int_{a_{\text{amin}}}^{a_{\text{max}}} dan_d(a) \Phi(a) V_{gr}(a) f_{\text{align}}(a)}.(28)$$

For grains in the diffuse ISM with  $a=0.05-0.25\,\mu\mathrm{m}$ , Draine & Hensley (2021) evaluated the starlight polarization efficiency integral by taking

$$\Phi(a) \approx \Phi(a_{\text{align}}) = \frac{3}{4\pi} \int \frac{Q_{\text{pol}}(a_{\text{align}}, \lambda)}{a_{\text{align}}} d\lambda, \quad (29)$$

which now only depends on the grain elongation. Consequently,

$$\begin{split} \frac{\Pi}{\sin^2 \gamma F_{\text{turb}}} &= \Phi(a_{\text{align}}) \int_{a_{\text{amin}}}^{a_{\text{max}}} dan_d(a) V_{gr}(a) f_{\text{align}}(a) \\ &= \Phi(a_{\text{align}}) V_d \langle f_{\text{align}} \rangle, \end{split} \tag{30}$$

where

$$\langle f_{\text{align}} \rangle = \frac{\int_{a_{\text{min}}}^{a_{\text{max}}} da(4\pi a^3/3) n_d(a) f_{\text{align}}(a)}{V_d}, \quad (31)$$

is the mass-weighted alignment efficiency and  $V_d = \int (4\pi a^3/3) n_d(a) da$  is the total dust volume per H atoms. The observed starlight polarization integral becomes

$$\Pi = \Phi(a_{\text{align}}) V_d \langle f_{\text{align}} \rangle \sin^2 \gamma F_{\text{turb}}, \tag{32}$$

which yields the inclination angle

$$\sin^2 \gamma = \frac{\Pi}{\Phi(a_{\text{align}})V_d \langle f_{\text{align}} \rangle F_{\text{turb}}}.$$
 (33)

# 3. SYNTHETIC OBSERVATIONS OF STARLIGHT POLARIZATION USING MHD SIMULATIONS

In real observations, the properties of local gas, dust, and magnetic fields change along the LOS due to the turbulent nature of the ISM. Consequently, we need to test whether the analytical formula given by Equation 26 can adequately describe the observed starlight polarization to verify the capability of inferring the inclination angle of the magnetic field using starlight polarization efficiency in such an inhomogeneous environment. In this study, we will post-process MHD simulations with our updated POLARIS code to obtain the synthetic starlight polarization. We will then apply our technique to infer B-field inclination angles using the synthetic observations.

### 3.1. MHD simulation datacube

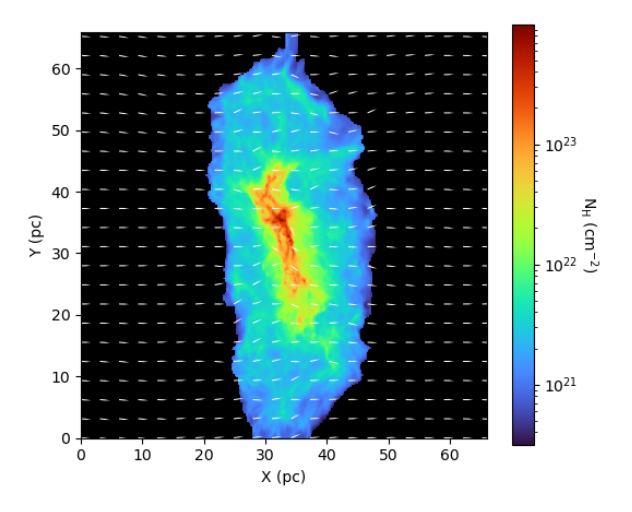
Following Hoang & Truong (2024), we reuse the snapshot of the evolution of a filamentary cloud under the effects of self-gravitating and B-fields taken from the magnetohydrodynamic (MHD) simulations by Ntormousi & Hennebelle (2019). The filamentary cloud was set up with a length of 66 pc and an effective thickness of 33 pc onto a three-dimensional data cube of  $256^3$  pixels. The initial mean B-field has a strength of  $B = 5\mu G$  and is perpendicular to the filament axis.

The left panel of Figure 3 shows the map of gas column density and the B-field morphology represented by the white segments, while the right panel demonstrates the linear relation between the gas column density  $N_{\rm H}$  and the optical extinction  $A_{\rm V}$  measured at  $\lambda=0.55\,\mu{\rm m}$ . The gas column density changes significantly within the filament, from  $N_{\rm H}\sim 10^{21}-10^{22}~{\rm cm}^{-2}$  in the outer region to  $N_{\rm H}\sim 4-5\times 10^{23}~{\rm cm}^{-2}$  in the central region, corresponding to the increase in visual extinction from  $A_{\rm V}\sim 1-10$  to  $A_{\rm V}>100$ . The variation of gas column density is expected to cause the variation of grain alignment and directly affect the observed starlight polarization and the results of inferred inclination angles of mean B-fields (see, e.g., Whittet et al. 2008; Andersson et al. 2015; Vaillancourt et al. 2020; Hoang et al. 2021).

The effect of magnetic turbulence is significant within the filamentary cloud, as the local B-fields are highly tangled in the denser part of the cloud with a high dispersion angle  $\delta\theta > 50^\circ$  (see Hoang & Truong 2024). We retake the magnetic turbulence factor  $F_{\rm turb}$  analyzed from the MHD data by Hoang & Truong (2024) and include it in the calculation of the starlight polarization efficiency and the inferred inclination angles.

# 3.2. Dust and Grain Alignment Models

In this work, we use the Astrodust model of interstellar dust in which silicate and carbonaceous components are well mixed together within one single dust population from Draine & Hensley (2021). The grain size distribution is assumed to follow the Mathis-Rumpl-Nordsieck size distribution described by the power law of  $dn \propto Ca^{-3.5}da$  in the range of grain sizes from  $a_{\rm min}=5\,{\rm nm}$  to  $a_{\rm max}=0.25\,\mu{\rm m}$  (Mathis et al. 1977). The grain shape is considered to be oblate spheroid with an axial ratio of 1.4, which was previously constrained through the starlight polarization observation in the ISM environment (Hensley & Draine 2023). We



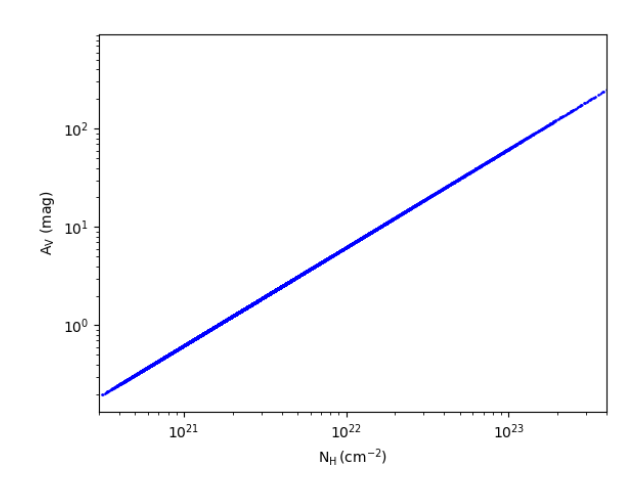


Figure 3. Left panel: The map of gas column density  $N_{\rm H}$  of a filamentary cloud taken from the MHD simulations by Ntormousi & Hennebelle (2019). The white segments demonstrate the B-field morphology perpendicular to the filament axis. Right panel: The linear correlation between the column density  $N_{\rm H}$  and the optical extinction  $A_{\rm V}$  derived from the updated POLARIS.

take the cross-sections for this oblate shape from Draine & Hensley (2021).  $^1$ 

We examine the effect of grain alignment on the synthetic starlight polarization and the inferred inclination angle by considering different grain alignment models as (1) Ideal RAT and (2) MRAT with different grain magnetic properties. For the radiation field, we consider grains to be irradiated by only the ISRF, which is described by the average radiation field in the solar neighborhood (Mathis et al. 1977). Grains can then be aligned by RATs with the exponential alignment degree as shown in Equation 22, which is first implemented in the updated POLARIS. For grain magnetic properties, we consider both PM grains with the fraction of iron of  $f_p = 0.1$ , and SPM grains with increasing levels of iron inclusion  $N_{\rm cl}$  from 50 to 10<sup>3</sup>. The SPM grains are expected to achieve more efficient magnetic alignment than PM grains due to higher magnetic susceptibility, according to the MRAT mechanism (Hoang & Lazarian 2016a, see also in Equation 19 - 21).

Note that the presence of grain growth can significantly affect the multi-band starlight polarization, especially toward dense regions (e.g., Whittet 2003; Vaillancourt et al. 2020; Hoang et al. 2021). We consider the variation of the maximum grain size from  $a_{\rm max}=0.25\,\mu{\rm m}$  to  $a_{\rm max}=1\,\mu{\rm m}$  and quantify their impact on the synthetic starlight polarization and the in-

Table 1. Grain alignment models considered.

Model	Aligned Sizes	Parameters
Ideal RAT MRAT	$[a_{ m align}, a_{ m max}]$ $[a_{ m align}, a_{ m max}]$	$R = 1$ PM, $f_p = 0.1$
	$[a_{ m align}, a_{ m max}]$	SPM, $N_{\rm cl} = 50, 10^3$

ferred inclination angles from the multi-wavelength polarization efficiency.

# 3.3. Modeling synthetic polarization from background stars

To model the polarization of background stars, we first place a plane of unpolarized background stars with  $N = 256 \times 256$  behind the filamentary cloud. Each background source is considered to be a blackbody radiating at an effective temperature  $T_{\rm eff} = 5000\,{\rm K}$ . We assume that they are located at a long distance from the cloud so that their radiation does not affect the alignment of grains inside the cloud, which is determined by the interstellar radiation field only. We then model the synthetic polarization of background stars due to dichroic extinction by aligned grains at multi-bands in the Johnson-Cousin photometric system from optical (e.g., B-band:  $\lambda_{\rm B}=0.45\,\mu{\rm m};$  V-band:  $\lambda_{\rm V}=0.55\,\mu{\rm m};$ R-band:  $\lambda_{\rm R} = 0.68 \,\mu{\rm m}$ ) to NIR wavelengths (e.g., Jband:  $\lambda_{\rm J} = 1.22 \,\mu{\rm m}$ ; H-band:  $\lambda_{\rm H} = 1.63 \,\mu{\rm m}$ ; K-band:  $\lambda_{\rm K} = 2.19 \,\mu{\rm m}$ ).

The RAT alignment physics was implemented in the POLARIS code by Reissl et al. (2016), whereas the MRAT mechanism was recently incorporated in the updated version by Giang et al. (2023). Here, we use the

 $<sup>^1</sup>$  The variation of the grain elongation could directly affect both the starlight polarization efficiency  $P/N_{\rm H}$  and the results of inferred inclination angles (see Appendix A for different grain axial ratios).

latest version of POLARIS code by Giang et al. (2023) for our numerical studies. For a detailed description of the implementation of RAT alignment physics and polarized radiative transfer, please see Reissl et al. (2016). For a detailed description of the alignment model parameters, see Giang et al. (2023).

# 4. NUMERICAL RESULTS

# 4.1. Polarization Coefficient Fraction $f_{pol}(\lambda)$

Figure 4 shows the fraction of linear polarization coefficient  $f_{\rm pol}(\lambda)$  as a function of wavelength measured from the outer to the inner regions of the cloud with increasing  $N_{\rm H}$ , considering the Ideal RAT alignment model. In the outer region, the fraction  $f_{\rm pol}(\lambda)$  around 0.8 - 0.9, but cannot achieve to 1 since only grains larger than  $a_{\rm align}$  can be aligned by RATs. Toward the inner region with  $N_{\rm H}>10^{22}$  cm<sup>2</sup>, only large grains  $a>0.1\,\mu{\rm m}$  can be aligned due to the increased gas randomization and the attenuated of ISRF (i.e., larger  $a_{\rm align}$ , see Equation 17). This results in the reduction of the alignment efficiency and a significant decrease in  $f_{\rm pol}(\lambda)$  to 0.1-0.2, and the peak  $f_{\rm pol,peak}$  tends to be shifted to longer wavelengths  $\lambda \sim 0.5-1\,\mu{\rm m}$ .

The effect of grain growth significantly affects the calculation of  $f_{\rm pol}(\lambda)$ , as illustrated in Figure 4 with the increasing maximum grain sizes from  $a_{\rm max}=0.25\,\mu{\rm m}$  (left panel) to  $a_{\rm max}=1\,\mu{\rm m}$  (right panel). With increasing  $a_{\rm max}$ , a higher population of aligned large grains  $a>0.25\,\mu{\rm m}$  contributes to the enhancement of the alignment efficiency, particularly in the inner dense cloud. As a result, the fraction  $f_{\rm pol}(\lambda)$  increases strongly to  $\sim 0.8-0.9$  in this region and the peak  $f_{\rm pol,peak}$  is shifted further to NIR wavelengths  $\lambda>1\,\mu{\rm m}$ .

The fraction of linear polarization coefficient  $f_{\rm pol}(\lambda)$  also depends on the grain magnetic properties. Figure 5 shows the maps of  $f_{\rm pol}$  calculated at V-band and K-band for different alignment models from PM to SPM grains with increasing levels of iron inclusion  $N_{\rm cl}$ . For PM grains, they are aligned by RATs with a lower alignment degree  $f_{\rm align}(a) \sim 0.475$  (see Section 2.2.2), then the fraction  $f_{\rm pol}(\lambda)$  is considerably low with  $\langle f_{\rm pol} \rangle_{\rm max} \sim 0.4 - 0.5$ . For SPM grains with high levels of embedded iron, they can achieve perfect magnetic alignment by MRAT with a higher alignment degree  $f_{\rm align}(a) \sim 1$ . Consequently, the total  $f_{\rm pol}(\lambda)$  increases to the maximum value of 0.8 - 0.9 as increasing levels of iron inclusions to  $N_{\rm cl} = 10^3$  - close to the maximum value achieved in the Ideal alignment case.

# 4.2. Synthetic Starlight Polarization Maps

Figure 6 shows the maps of the intrinsic polarization efficiency  $P_{\text{ext,i}}/N_{\text{H}}$  in which all grain sizes are per-

fectly aligned within the cloud and the magnetic fields are lying on the POS (i.e.,  $\sin^2 \gamma = 1$ ), calculated at multi-wavelength bands from optical (i.e., B-, V- and R-bands) to NIR (i.e., J-, H- and K-bands). The intrinsic polarization efficiency is constant in the outer part of the cloud with  $N_{\rm H} < 10^{22}~{\rm cm}^{-2}$ , and decreases with increasing observed wavelength. However, in the densest part of the cloud, most radiation from background stars is highly absorbed, then the polarization efficiency significantly decreases to the lower values of  $P_{\rm ext,i}/N_{\rm H} < 10^{-21}\,\%~{\rm cm}^2$ .

Figure 7 shows the variation of the intrinsic fractional polarization  $P/\tau_{\lambda}$  calculated from optical to NIR wavelengths with respect to the column density  $N_{\rm H}$ . The extinction effect on the fractional polarization becomes stronger in the denser region, especially at optical bands  $\lambda \sim 0.4-0.6\,\mu{\rm m}$  with a considerable drop in  $P/\tau_{\lambda}$  at the transition column density  $N_{\rm H,trans} \approx 10^{22}~{\rm cm}^{-2}$  with the slope of  $\sim 1$ . At NIR wavelengths  $\lambda \sim 1.2-2.2\,\mu{\rm m}$ , the starlight radiation is less extinct by dust grains. Consequently, the starlight polarization can be traced toward the densest part of the cloud, and the extinction effect is only significant at  $N_{\rm H} > N_{\rm H,trans} \sim 10^{23}~{\rm cm}^{-2}$  with the shallower slope of  $\sim 0.6-0.8$ .

Figure 8 shows the maps of the synthetic starlight polarization efficiency  $P_{\rm syn}/N_{\rm H}$  when the Ideal RAT alignment model is taken into account. The variation of fractional polarization with increasing gas column density is illustrated in the left panel of Figure 9. Compared with the intrinsic ones, the values  $P_{\rm syn}/N_{\rm H}$  are lower induced by a fraction of aligned grains  $a>a_{\rm align}=0.02-0.1\,\mu{\rm m}$ . The loss of grain alignment is dominant in the denser region with  $N_{\rm H,trans}\sim10^{22}~{\rm cm}^{-2}$ , resulting in a significant decrease in the fractional polarization at all optical-NIR wavelengths with the slope of  $\sim1$ .

To examine whether the inclination angles can be inferred from the multi-band polarization efficiency, we calculate the polarization efficiency from the analytical model as shown in Equation 26, giving the multi-band intrinsic polarization efficiency in Figure 6, the mean fraction  $f_{\rm pol}(\lambda)$  determined from our numerical calculations at optical-NIR wavelengths, the mean inclination angles  $\sin^2 \gamma$  and the magnetic turbulence factor  $F_{\rm turb}$  derived from the MHD simulation. We then compare with the synthetic polarization efficiency generated by the updated POLARIS, as illustrated in the right panel of Figure 9 at both optical and NIR bands. One can see that the analytical values are well correlated with the synthetic ones at all optical-NIR wavelengths.

# 4.3. Inferred inclination B-field angles from starlight polarization efficiency

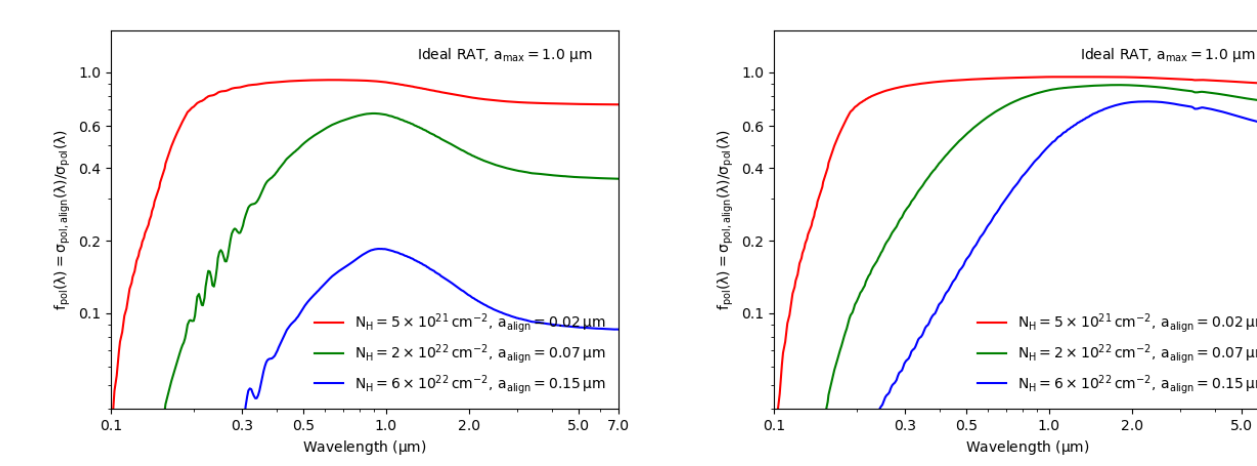


Figure 4. The wavelength-dependent fraction of linear polarization coefficient  $f_{\rm pol}(\lambda)$  calculated from the outer to the inner cloud with increasing column density  $N_{\rm H}$ , considering the grain growth effect with increased maximum grain size from  $a_{\rm max} = 0.25 \,\mu{\rm m}$  to  $a_{\rm max} = 1 \,\mu{\rm m}$ . The Ideal RAT alignment model is being assumed. The fraction  $f_{\rm pol}$  is lower in the inner dense cloud under the effect of grain alignment loss by gas randomization and the peak of  $f_{\rm pol}(\lambda)$  tends to be shifted to longer wavelengths.

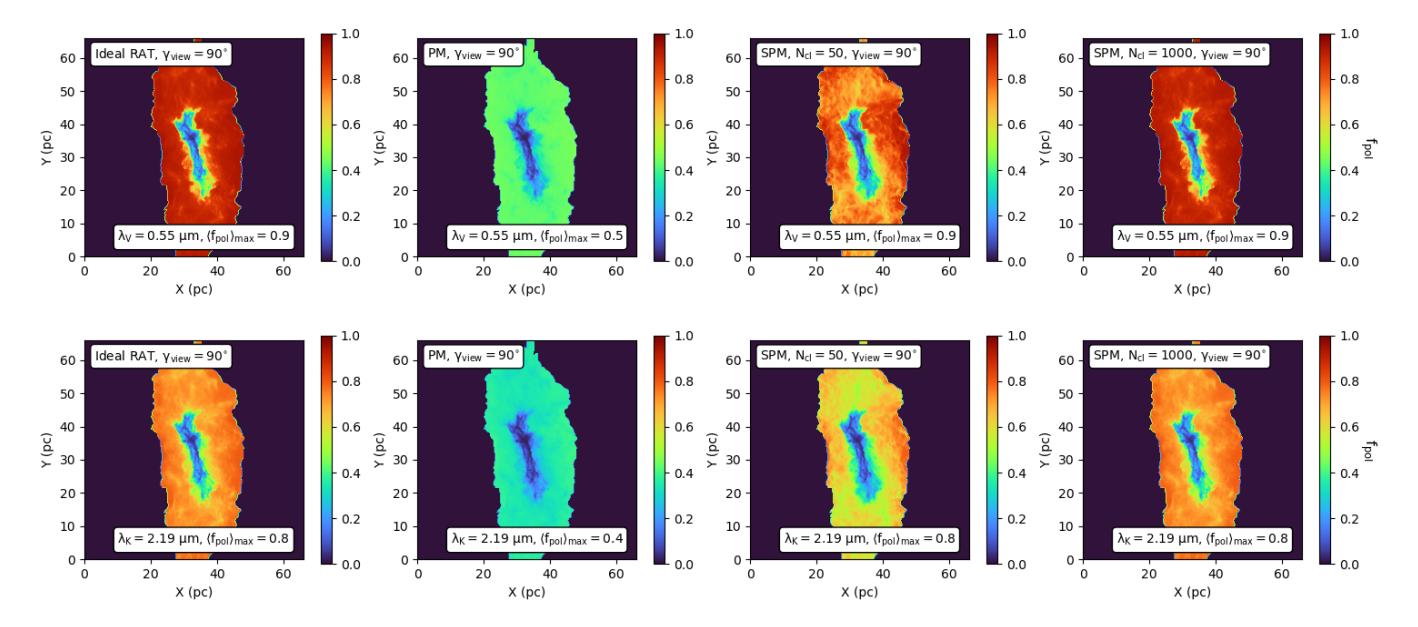


Figure 5. The maps of the fraction of polarization coefficient  $f_{\rm pol}$  calculated at V-band (i.e.,  $\lambda_{\rm V}=0.55\,\mu{\rm m}$ , top panels) and K-band (i.e.,  $\lambda_{\rm V}=2.19\,\mu{\rm m}$ , bottom panels) for different alignment models from Ideal RAT to MRAT alignment with PM and SPM grains with  $N_{\rm cl}=50,1000$ . The fraction  $f_{\rm pol}$  is lower for paramagnetic grains due to a lower alignment degree, and can be enhanced when grains have high levels of iron inclusion  $N_{\rm cl}>50$ .

In Section 4.2, we show the analytical model of polarization efficiency can well describe the synthetic polarimetric data. We now apply the analytical model to calculate the inclination angles inferred from optical-NIR polarization efficiency  $P/N_{\rm H}$  as presented in Equation 27. We also discuss the major effects on the polarization efficiency and the inferred inclination angles as (1) the contribution of iron inclusions, (2) the viewing angles

between mean fields and the LOS, and (3) the impact of grain growth.

# 4.3.1. Using multi-wavelength starlight polarization efficiency

Figure 10 shows the maps of the inferred inclination angles  $\gamma_{\rm syn}^{\rm star}$  from the optical-NIR starlight polarization efficiency  $P_{\rm syn}/N_{\rm H}$  previously presented in Figure 8. The colored contours illustrate the cloud regions where  $A_{\rm V}=3$  (black) and  $A_{\rm V}=30$  (blue). Figure 11 demonstrates

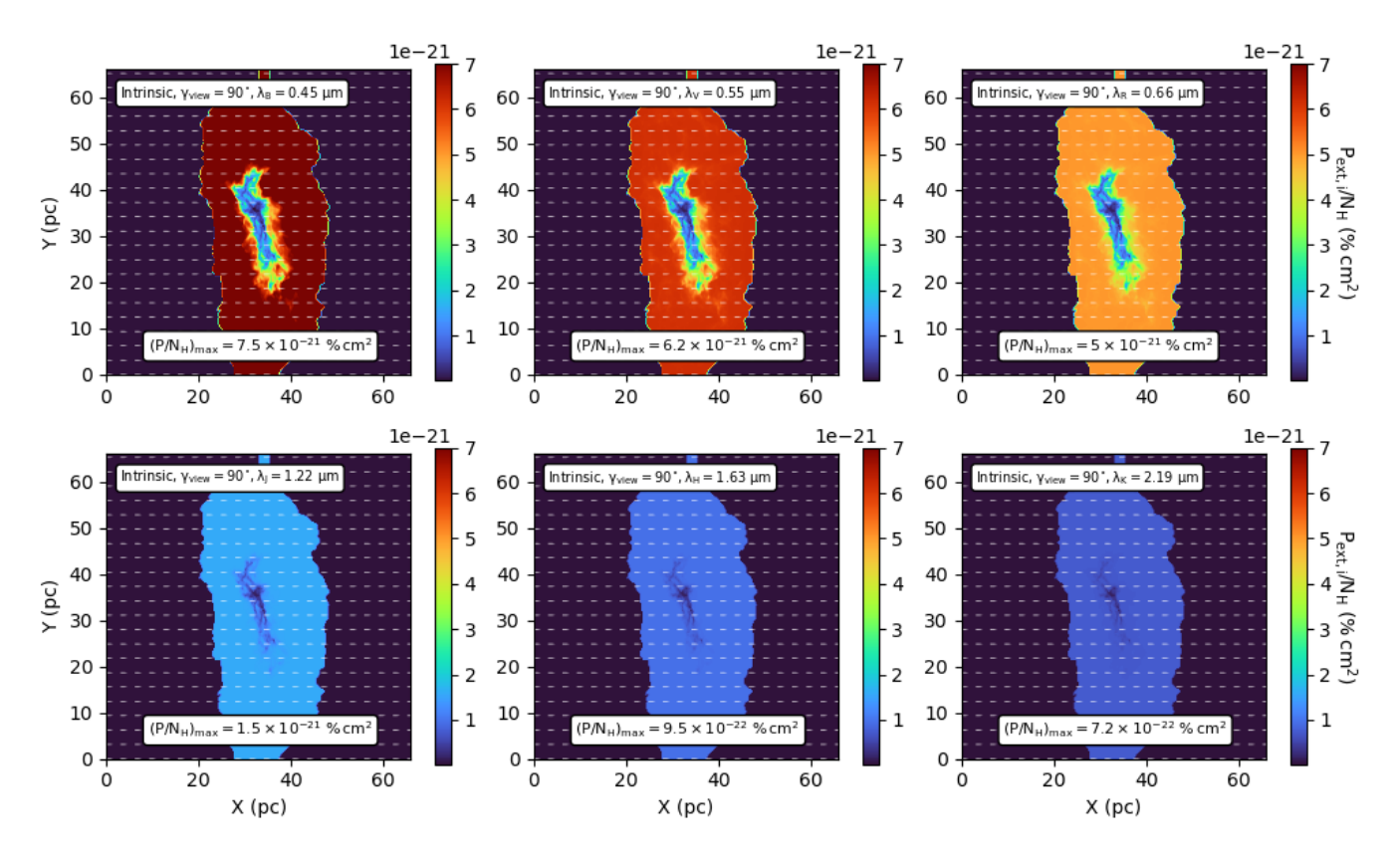


Figure 6. The maps of the intrinsic polarization efficiency  $P_{\rm ext,i}/N_{\rm H}$  at optical-NIR bands  $\lambda = 0.45 - 2.19 \,\mu{\rm m}$ . The polarization efficiency is constant in the outer cloud but decreases toward the inner dense cloud resulting from the high extinction effect.

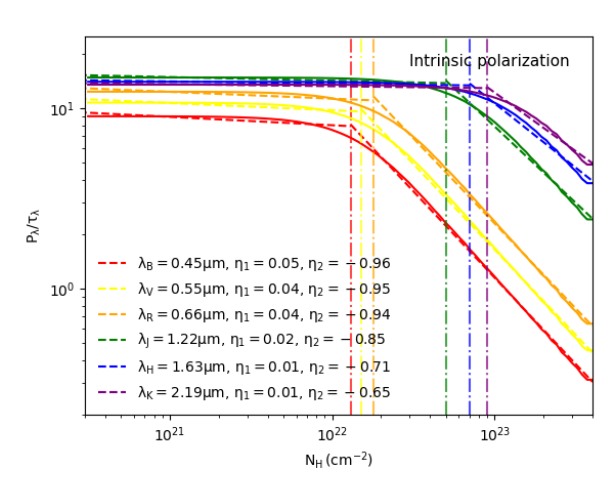


Figure 7. The variation of the fractional polarization  $P_{\lambda}/\tau_{\lambda}$  with respect to the gas column density  $N_{\rm H}$ . The polarization of background stars can be traced in the less dense cloud with  $N_{\rm H} < 10^{22}~{\rm cm}^{-2}$  at optical bands due to the impact of high dust extinction, and could be traced further to the denser region  $N_{\rm H} \sim 10^{23}~{\rm cm}^{-2}$  when being observed at NIR bands.

strates the orientation of 3D B-fields derived from the inferred inclination angles  $\gamma_{\rm syn}^{\rm star}$ , in comparison with the true 3D B-fields from MHD data. One can obtain that at

optical bands such as B-, V- and R-bands (top row), the inclination angles of the mean B-fields can only be traced in the outer part of the cloud  $N_{\rm H} < 5 \times 10^{21}~{\rm cm^{-2}}$  (i.e.,  $A_{\rm V} < 3$ ) with  $\gamma_{\rm syn}^{\rm star} \sim 75-80$  degrees. Meanwhile, the inclination angle maps return more NAN values toward the inner part of the cloud due to the combined effects of dust extinction, grain alignment loss, and stronger magnetic turbulence. The inferred inclination angles can be traced further to the denser region with  $N_{\rm H}$  up to  $5 \times 10^{22}~{\rm cm^{-2}}$  (i.e.,  $A_{\rm V} \approx 30$ ) when being observed at NIR wavelengths (bottom row), and tends to decrease to  $\sim 40-60$  degrees as a result of self-gravity and magnetic turbulence in this region.

We then quantify our main method by comparing the inferred inclination angles from the synthetic starlight polarization efficiency with the true inclination angles of the mean B-fields derived from the MHD simulation. For each cell of the simulation box, the true inclination angles of B-fields are defined as

$$\sin \gamma_{\mathbf{B}_{(\mathbf{i},\mathbf{j},\mathbf{k})}} = \sqrt{\frac{B_{x_{(\mathbf{i},\mathbf{j},\mathbf{k})}}^2 + B_{y_{(\mathbf{i},\mathbf{j},\mathbf{k})}}^2}{|B|_{(\mathbf{i},\mathbf{j},\mathbf{k})}^2}},$$
 (34)

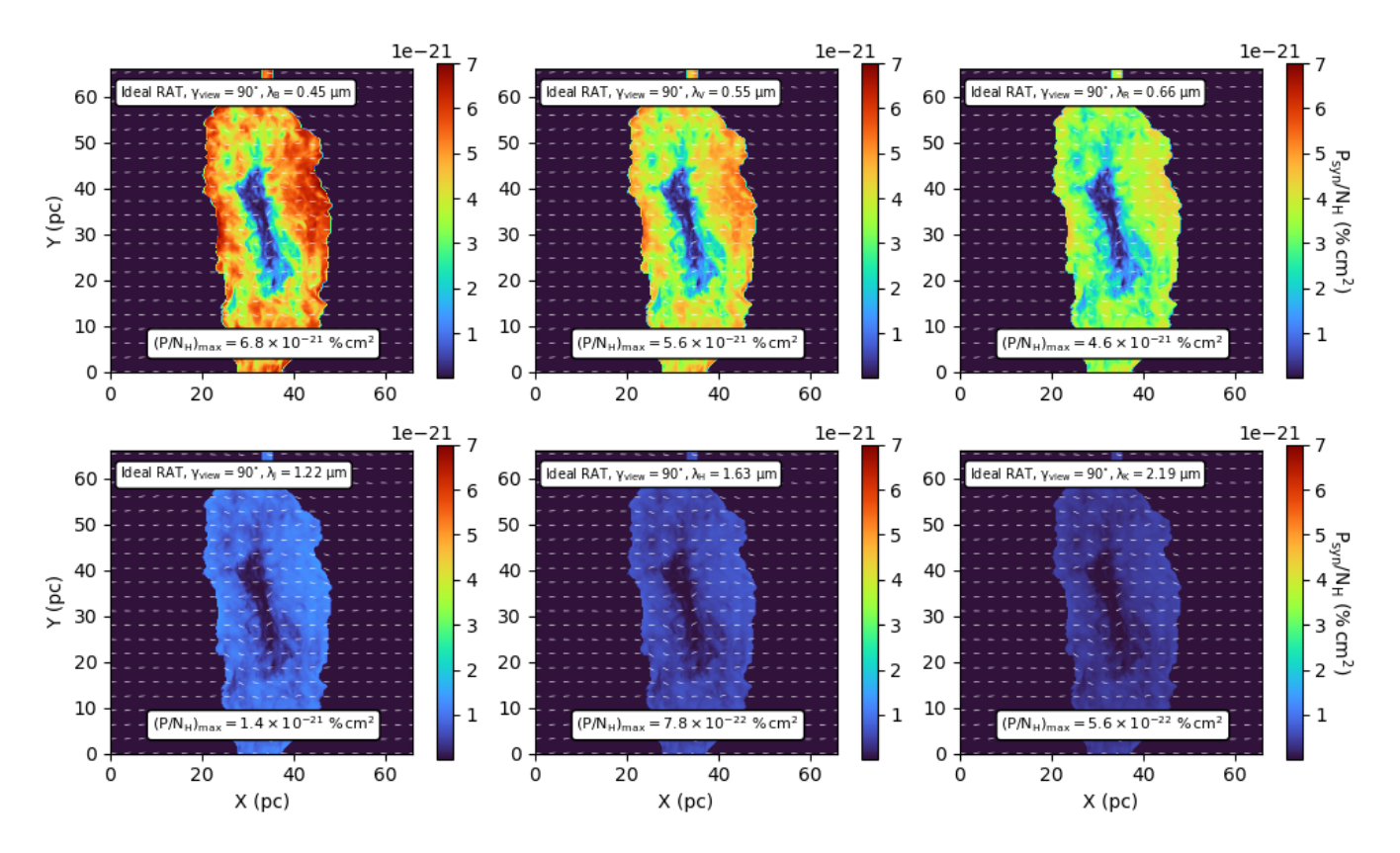


Figure 8. Similar to Figure 6 for the synthetic polarization efficiency  $P_{\text{syn}}/N_{\text{H}}$  but when the Ideal RAT alignment is taken into consideration. The loss of grain alignment by strong gas randomization causes a significant decrease in the polarization efficiency in the denser region.

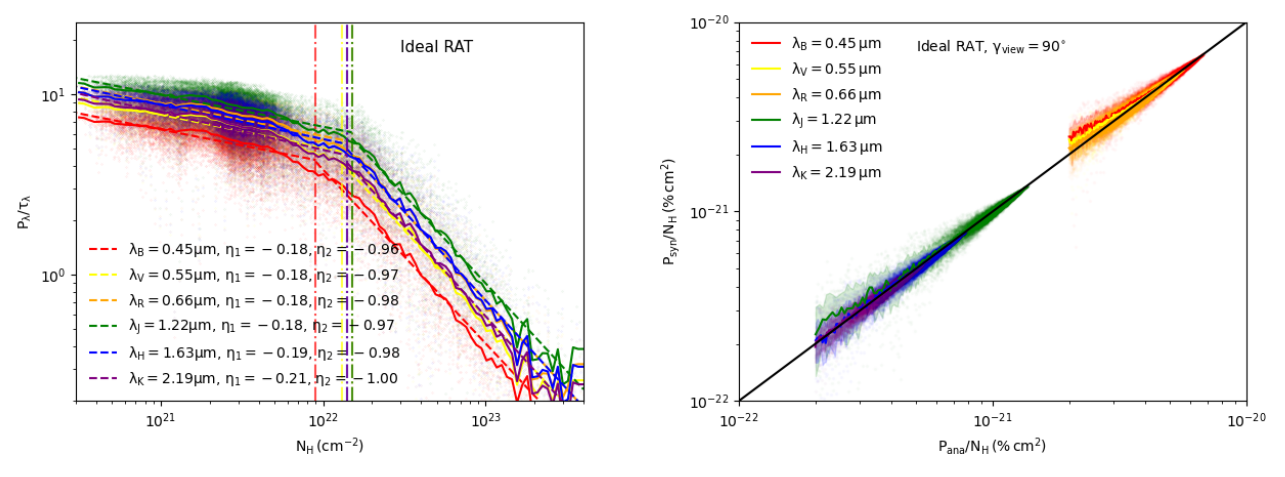


Figure 9. Left panel: The fractional polarization  $P_{\lambda}/\tau_{\lambda}$  versus  $N_{\rm H}$  when considering the Ideal RAT alignment model. The effect of grain alignment loss results in a decrease in fractional polarization when  $N_{\rm H} > 10^{22}~{\rm cm}^2$  for all wavelengths with the slope of  $\sim 1$ . Right panel: Synthetic polarization efficiency  $P_{\rm syn}/N_{\rm H}$  from numerical calculations versus the analytical values  $P_{\rm ana}/N_{\rm H}$  derived from Equation 26. The analytical values are in agreement with the synthetic data at both optical and NIR bands.

and the mean inclination angle is calculated by

$$\sin \langle \gamma_{\rm B} \rangle = \sqrt{\frac{\overline{B_x^2} + \overline{B_y^2}}{|B|^2}}.$$
 (35)

The inferred inclination angles can also be compared with the density-weighted of the mean inclination angle along the LOS, denoted by  $\gamma_{\rho}$ , which is determined by

$$\sin \gamma_{\rho} = \sqrt{\frac{\int_{\text{LOS}} n_{\text{H}} \sin^2 \gamma_{\text{B}_{(i,j,k)}} dz}{\int_{\text{LOS}} n_{\text{H}} dz}},$$
 (36)

where  $\gamma_{B_{(i,j,k)}}$  are the local inclination angles derived from Equation 34.

Figure 12 shows the distribution of the inferred inclination angles  $\gamma_{\rm syn}^{\rm star}$  from our technique using the polarization efficiency  $P/N_{\rm H}$  calculated at optical and NIR wavelengths (solid color lines), compared with the true angles (solid black line) and the density-weighted angles (dashed black line). Table 2 summarizes the most probable values of the inclination angle from our technique and the true values from the MHD simulation. Despite the sensitive dependence on the wavelength, the results are quite close to the mean inclination angles from the MHD data with the differences of only 2 - 6 degrees.

# 4.3.2. Effect of iron inclusions

The presence of iron inclusions inside grains enhances the magnetic alignment by MRAT (see Hoang & Lazarian 2016a) and the synthetic results of polarization efficiency  $P_{\text{syn}}/N_{\text{H}}$ . Figure 13 and 14 shows the polarization efficiency at V-band and K-band, considering Realistic alignment models as (1) PM grains (second row) and (2) SPM grains with  $N_{\rm cl} = 50$  (third row) and  $N_{\rm cl} = 1000$  (last row), compared with the Ideal RAT case (first row). Different viewing angles from  $\gamma_{\text{view}} = 0^{\circ}$ to  $\gamma_{\text{view}} = 90^{\circ}$  are being assumed. For the models of PM grains, the polarization efficiencies at optical and NIR bands are significantly low due to a lower alignment efficiency. For SPM grains with increasing levels of iron inclusions, the polarization efficiency are being enhanced for all wavelengths and can recover to the Ideal RAT case when  $N_{\rm cl} = 50 - 1000$ .

The comparison between the analytical polarization efficiency and the synthetic values for both Ideal RAT and Realistic alignment models are illustrated in the left panels of Figure 15 at V-band (top) and K-band (bottom), assuming  $\gamma_{\rm view} = 90^{\circ}$ . For all alignment models, the analytical calculations are in agreement with the synthetic polarimetric data.

Figure 16 shows the inferred inclination angle maps extracted from the starlight polarization efficiency at V-band for different alignment models and viewing angles

 $\gamma_{\rm view}$ . Figure 17 shows the same, but tracing toward the denser region of the cloud  $A_{\rm V}=30$  when being observed at K-band. For PM grains, the inclination angle maps return more NAN values due to the reduced alignment efficiency with small  $f_{\rm pol}<0.4-0.5$  (see Figure 5). The situation can be resolved when grains have high levels of iron inclusion with a higher fraction  $f_{\rm pol}\sim0.8-0.9$  due to the efficient alignment by MRAT, which results in fewer NAN values.

The histogram of the inferred inclination angles  $\gamma_{\rm syn}^{\rm star}$  obtained from the starlight polarization at V- and K-bands for different grain alignment models and viewing angles in comparison with the mean inclination angles from the MHD data are illustrated in Figure 18, while the peak values of the distribution are presented in Table 3. One can obtain that the results from our method are insensitive to grain alignment models, and less different than the true values from the MHD simulation.

### 4.3.3. Effect of viewing angles

The viewing angle  $\gamma_{\text{view}}$  between the mean B-fields and the LOS can directly impact the calculation of the polarization efficiency  $P_{\text{syn}}/N_{\text{H}}$ , as illustrated in both Figure 13 and 14. For small  $\gamma_{\text{view}}$  (i.e., magnetic fields are along the LOS), the projection effect by the inclined cloud-scale B-fields is significant, resulting in a much lower polarization efficiency. The total polarization efficiency in the entire cloud increases significantly as the mean B-fields are perpendicular to the LOS with  $\sin^2 \gamma \sim 1$  for larger  $\gamma_{\text{view}}$ . And the synthetic results are well correlated with the analytical calculations, as illustrated in the right panels of Figure 15 for various viewing angles.

The impact of viewing angles  $\gamma_{\text{view}}$  on the calculation of the inferred inclination angles retrieved from  $P_{\text{syn}}/N_{\text{H}}$  are also shown in Figure 16 and 17. The inclination angle maps return fewer NAN values when  $\gamma_{\text{view}}$  is small and the mean B-field inclination angle effect dominates. For large  $\gamma_{\text{view}}$ , the magnetic turbulence effect is more dominant in the POS. This leads to more NAN values, particularly in the denser region of the cloud where the fluctuation of magnetic fields is stronger. In spite of these variations, the values of the inclination angle derived from our method are close to the true inclination angles from the MHD data in all cases of viewing angle, as shown in both Figure 18 and Table 3.

### 4.3.4. Effect of grain growth

In this section, we examine the major impact of grain growth on the synthetic polarization efficiency. Figure 19 shows the effect of grain growth on the intrinsic polarization efficiency  $P_{\rm ext,i}/N_{\rm H}$  at V-band and K-band, respectively, as the maximum grain size increases from

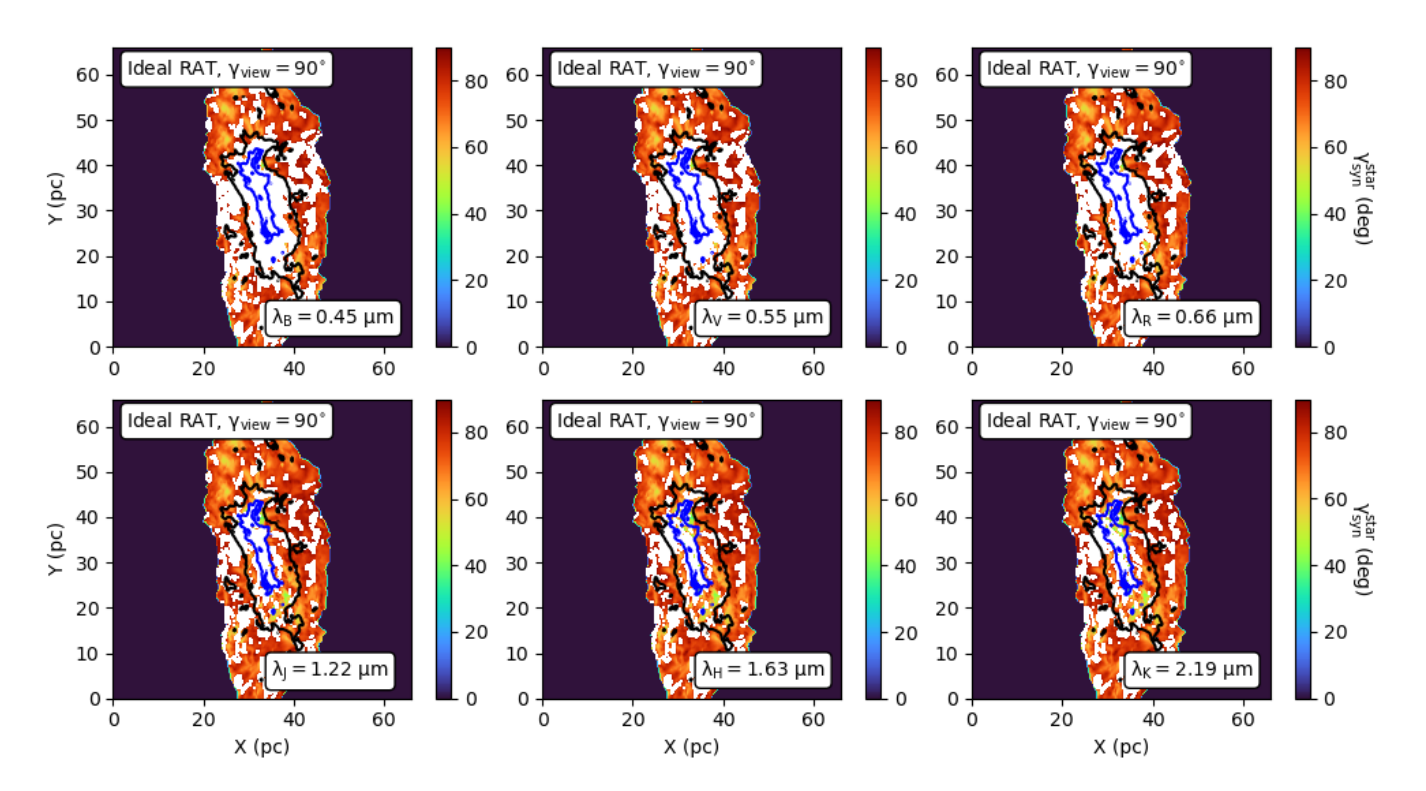


**Figure 10.** Maps of the inferred inclination angles  $\gamma_{\rm syn}^{\rm star}$  from the multi-band polarization efficiency  $P_{\rm syn}/N_{\rm H}$ , considering the Ideal RAT alignment model and  $\gamma_{\rm view}=90^{\circ}$ . At optical wavelengths, the inclination angles can be retrieved in the outer region of the cloud of  $N_{\rm H}<5\times10^{21}~{\rm cm}^{-2}$  (i.e.,  $A_{\rm V}<3$ , black contour), and can be inferred in the high-density region up to  $5\times10^{22}~{\rm cm}^{-2}$  (i.e.,  $A_{\rm V}=30$ , blue contour) when being observed at longer wavelengths.

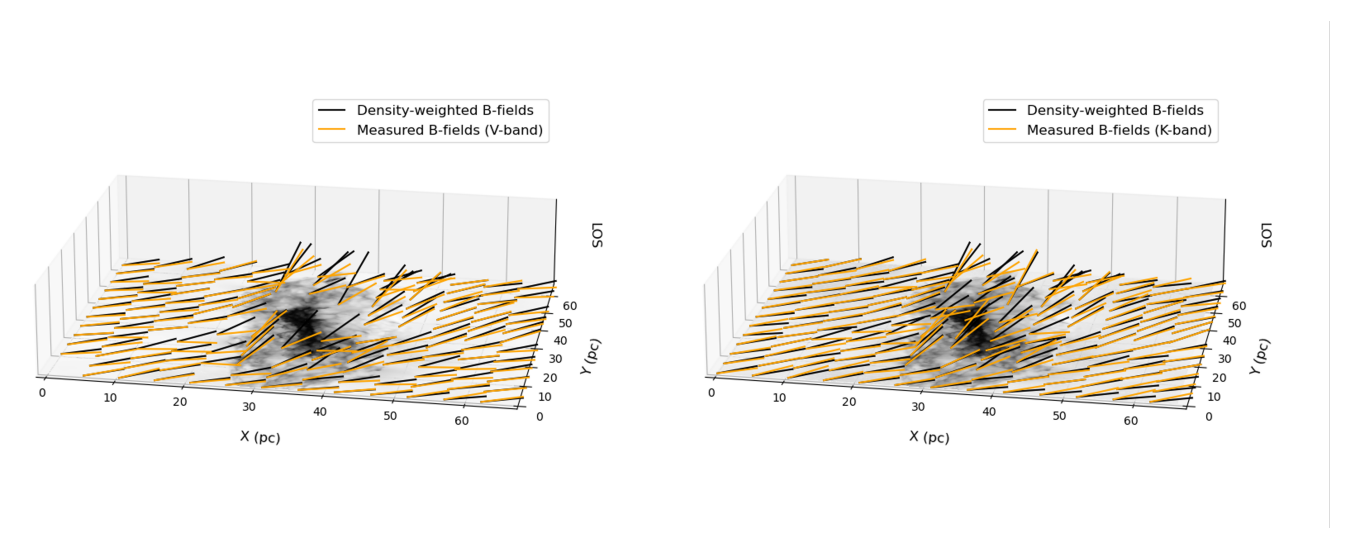


Figure 11. Illustrations of the 3D B-fields retrieved from the inclination angles  $\gamma_{\rm syn}^{\rm star}$  (orange lines) inferred from the starlight polarization efficiency at optical- (i.e.,  $\lambda_{\rm V}=0.55\,\mu{\rm m}$ , left panel) and NIR-bands (i.e.,  $\lambda_{\rm K}=2.19\,\mu{\rm m}$ , right panel), in comparison with the true 3D B-fields (black lines) derived from the density-weighted inclination angles  $\gamma_{\rho}$ . The starlight polarization efficiency maps  $P/N_{\rm H}$  are placed in the POS (i.e., XY-plane), while the third axis represents the LOS with no distance information.

Table 2. Summary of the most probable values (i.e., the peak inclination in the histograms) of the inclination angles derived from the starlight polarization efficiency  $P/N_{\rm H}$  at optical and NIR bands in comparison with the true inclination angles in MHD simulation.

$\langle \gamma_{ m B}  angle^{ar{\wedge}}$	$\gamma^{ar{\wedge}}_{ ho}$	$\gamma_{\mathrm{syn}}^{\mathrm{star,B}^{\wedge}}$	$\gamma_{\mathrm{syn}}^{\mathrm{star,V}^{\tilde{\wedge}}}$	$\gamma_{\mathrm{syn}}^{\mathrm{star,R}^{\wedge}}$	$\gamma_{\mathrm{syn}}^{\mathrm{star,J}^{\wedge}}$	$\gamma_{\mathrm{syn}}^{\mathrm{star,H}^{\wedge}}$	$\gamma_{ m syn}^{ m star, K^{\wedge}}$
77.01°	73.04°	78.45°	77.19°	77.91°	77.37°	77.37°	76.83°

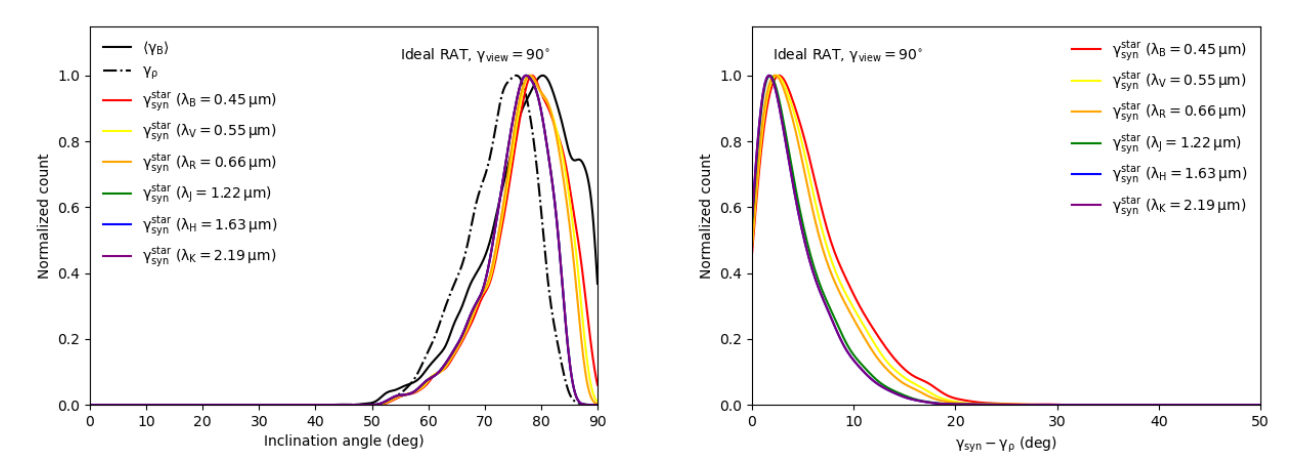


Figure 12. Left panel: Histogram of the inclination angles derived from our technique by using the polarization efficiency at optical-NIR wavelengths (solid color lines), compared with the true mean angles (solid black line) and the density-weighted angles (dashed black line) from the MHD data. Right panel: The difference between the inferred inclination angles and the density-weighted angles  $\gamma_{\text{syn}} - \gamma_{\rho}$ . The inferred inclination angles are insensitive to the wavelength with roughly 75 - 80 degrees.

Table 3. Same as Table 2 but for different grain alignment models and viewing angles  $\gamma_{\text{view}}$  between the LOS and the mean field.

$\gamma_{ m view}$	$\langle \gamma_{ m B}  angle^{ar{\wedge}}$	$\gamma_{ ho}^{ar{\wedge}}$	$\gamma_{ m syn,Ideal\ RAT}^{ m star,V}$	$\gamma_{\mathrm{syn,MRAT}}^{\mathrm{star,V}^{\wedge}}$ $(\mathrm{N_{cl}} = 50)$	$\gamma_{\rm syn,MRAT}^{\rm star,V^{\wedge}} $ $(N_{\rm cl} = 1000)$	$\gamma_{ m syn,Ideal\ RAT}^{ m star,K}$	$\gamma_{\mathrm{syn,MRAT}}^{\mathrm{star,K}^{\wedge}}$ $(\mathrm{N_{cl}} = 50)$	$\gamma_{\mathrm{syn,MRAT}}^{\mathrm{star,K}^{\wedge}}$ $(\mathrm{N_{cl}} = 1000)$
$0^{\circ}$	$11.36^{\circ}$	$29.4^{\circ}$	$23.62^{\circ}$	$24.34^{\circ}$	$23.62^{\circ}$	$25.61^{\circ}$	$23.98^{\circ}$	$25.79^{\circ}$
$30^{\circ}$	$38.4^{\circ}$	$42.38^{\circ}$	$42.56^{\circ}$	$42.38^{\circ}$	$42.56^{\circ}$	$42.38^{\circ}$	$42.02^{\circ}$	$42.38^{\circ}$
$60^{\circ}$	$67.81^{\circ}$	$60.6^{\circ}$	$64.75^{\circ}$	$67.09^{\circ}$	$64.57^{\circ}$	$63.84^{\circ}$	$66.37^{\circ}$	$64.02^{\circ}$
$90^{\circ}$	$77.01^{\circ}$	$73.04^\circ$	$77.19^{\circ}$	$79^{\circ}$	$77.19^{\circ}$	$76.83^{\circ}$	$81.34^{\circ}$	$76.65^{\circ}$

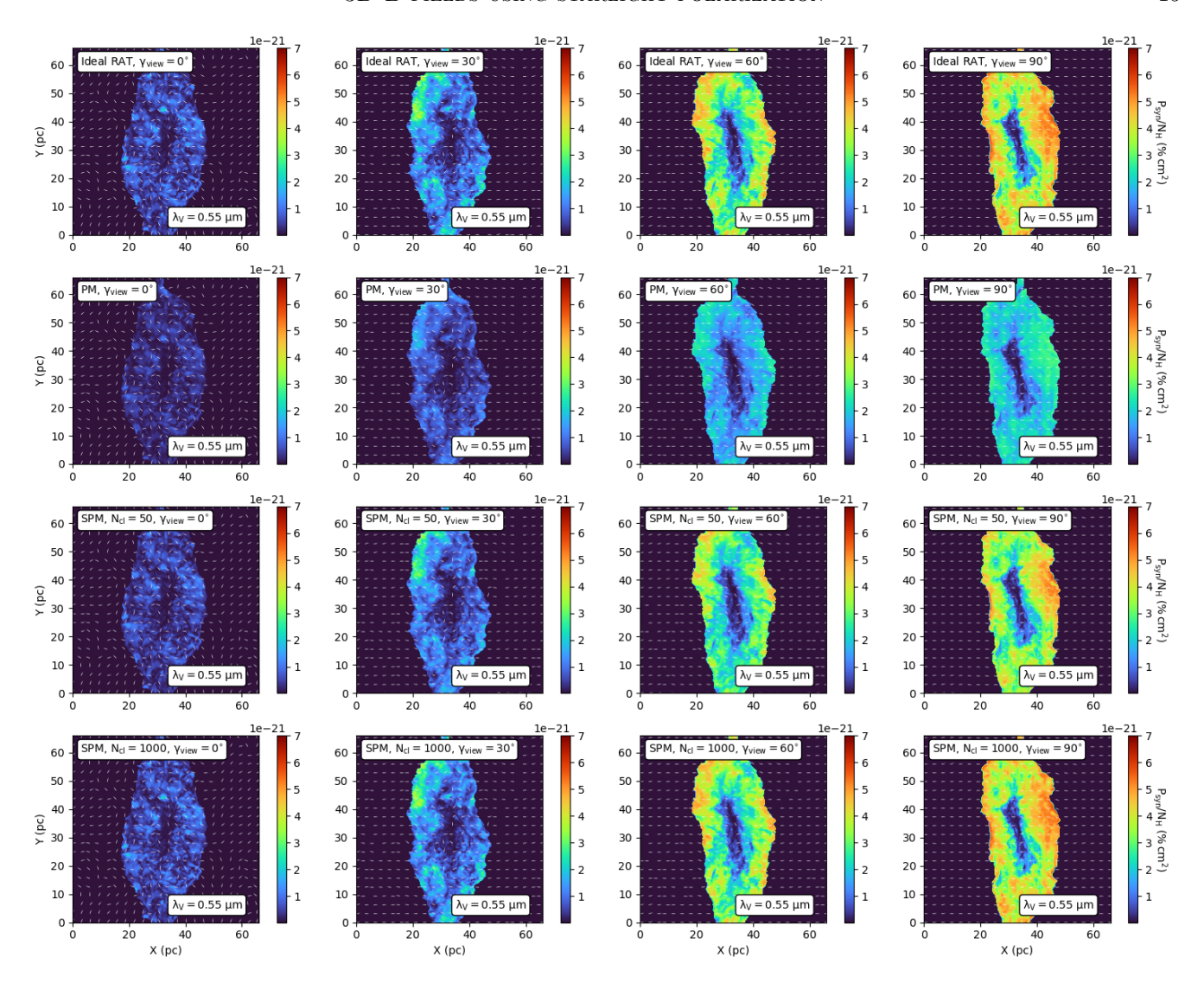


Figure 13. Maps of the synthetic polarization efficiency at V-band ( $\lambda_{\rm V}=0.55\,\mu{\rm m}$ ) for both Ideal RAT and Realistic models with PM and SPM grains, assuming different viewing angles  $\gamma_{\rm view}=0^{\circ},30^{\circ},60^{\circ}$  and  $90^{\circ}$ . The overall starlight polarization efficiency is much lower within the cloud when grains are paramagnetic and can be enhanced if grains have iron inclusions. The projection effect of the inclined B-fields causes the reduction of the polarization efficiency for small  $\gamma_{\rm view}$ , and increases when the mean B-fields are in the POS (i.e., larger  $\gamma_{\rm view}$ ).

 $a_{\rm max}=0.25\,\mu{\rm m}$  to  $a_{\rm max}=1\,\mu{\rm m}$ . With the contribution of a higher population of larger grains, the absorbed polarization of background stars is more prominent at NIR than at optical wavelengths, leading to an increase in the K-band intrinsic polarization efficiency and a significant reduction of V-band intrinsic polarization efficiency.

Figure 20 demonstrates the effect of grain growth on the variation of the V-band and K-band fractional polarization  $P_{\lambda}/\tau_{\lambda}$  within the filamentary cloud, assuming  $\gamma_{\rm view}=90^{\circ}$ . The increasing grain sizes cause the decrease in optical extinction and the increase in NIR extinction. Therefore, the transition column density  $N_{\rm H,trans}$  for the depolarization by extinction at V-band increases from  $10^{22}$  to  $2.5 \times 10^{22}$  cm<sup>-2</sup>, whereas that

transition value for K-band depolarization decreases from  $\sim 10^{23}$  to  $5\times 10^{22}~\rm cm^{-2}.$ 

Figure 21 shows similar but for the synthetic V-band and K-band polarization efficiency  $P_{\rm syn}/N_{\rm H}$  considering the Ideal RAT alignment, while the variation of fractional polarization within the filamentary cloud is illustrated in Figure 7. The presence of grain growth allows the alignment of larger grains in the inner dense region and produces higher polarization efficiency, especially at NIR wavelengths (see also in Figure 4). Therefore, the transition column density for grain alignment loss starts to be shifted to the denser part of the cloud. This effect is more prominent for K-band fractional polarization, which shows the change in the transition column density

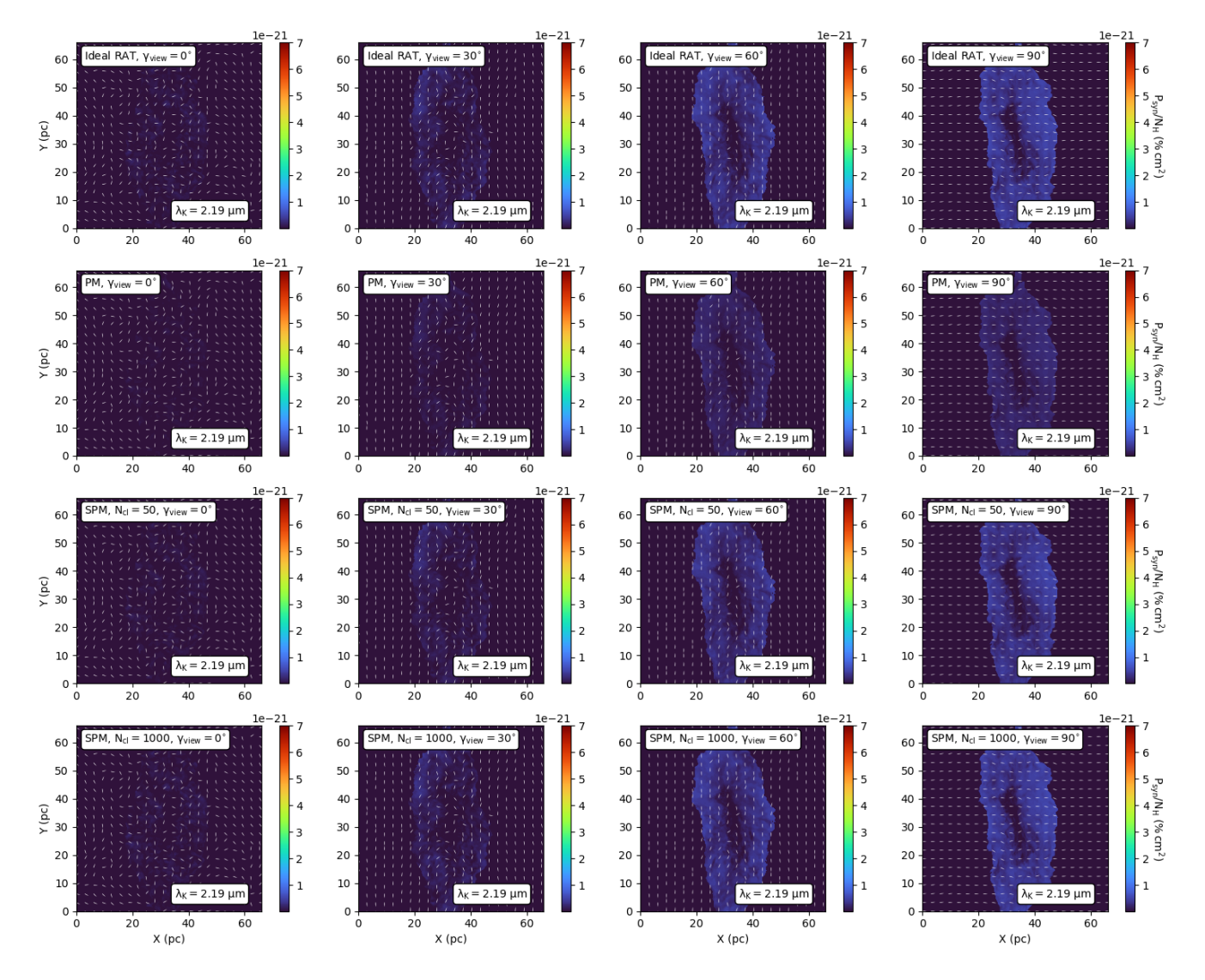


Figure 14. Similar to Figure 13 but when being observed at K-band ( $\lambda_{\rm K} = 2.19 \,\mu{\rm m}$ ) with a lower polarization efficiency.

from  $N_{\rm H,trans} \sim 10^{22}~{\rm cm}^{-2}$  to  $N_{\rm H,trans} \sim 3 \times 10^{22}~{\rm cm}^{-2}$  when the maximum grain size increases to  $1\,\mu{\rm m}$ .

Figure 23 shows the results of the inclination angles retrieved from the V-band and K-band polarization efficiency under the effect of grain growth, assuming the case of Ideal RAT alignment and  $\gamma_{\rm view}=90^\circ$ . Despite the impact of grain growth on grain alignment and the polarization efficiency within the filamentary cloud as shown in Figure 21, the results of inferred inclination angles from our method seem to be unchanged.

# 4.4. Inferred Inclination Angles Using Starlight Polarization Integral

As discussed in Section 2.3.2, the mean B-field inclination angles can potentially be retrieved from the observed starlight polarization integral  $\Pi_{\rm obs}$ . In this section, we present the synthetic results of the starlight

polarization integral  $\Pi_{\rm syn}$  and the derived inclination angles  $\gamma_{\rm syn}^{\rm spec}$  as shown in Equation 28.

### 4.4.1. Synthetic Starlight Polarization Integral

Figure 24 shows the starlight polarization efficiency integral  $\Phi(a)$  from the Astrodust model calculated over the size range from  $a_{\min}=5\,\mathrm{nm}$  to  $a_{\max}=1\,\mu\mathrm{m}$  (Draine & Hensley 2021). The integral is taken over the range of wavelength from  $\lambda_{\min}=0.15\,\mu\mathrm{m}$  (UV) to  $\lambda_{\max}=2.19\,\mu\mathrm{m}$  (NIR) where the starlight polarization is observably strong. The oblate shape is considered with increasing axial ratio s=1.4-3. One can see that the integral increases with increasing grain sizes and becomes saturated for grains with  $a\sim0.05-0.25\,\mu\mathrm{m}$ . For large grains  $a>0.25\,\mu\mathrm{m}$ , they mostly polarize starlight radiation in longer wavelengths  $\lambda>1\,\mu\mathrm{m}$ , then the value of  $\Phi(a)$  significantly drop to < 0.4. And the polarization efficiency integral is higher to  $\Phi(a)\sim2-4$  when

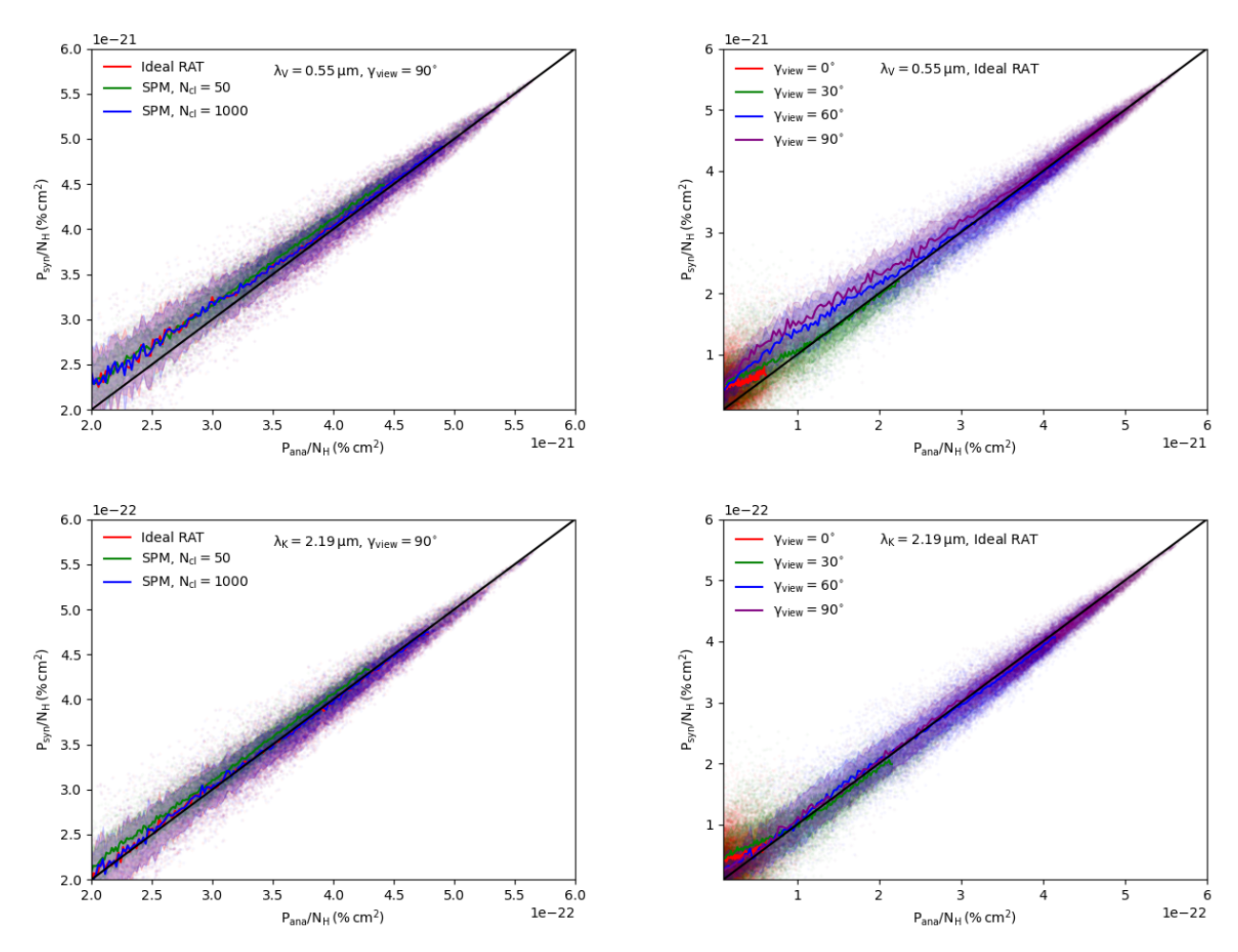


Figure 15. The comparison of the synthetic starlight polarization efficiency  $P/N_{\rm H}$  at V-band (top) and K-band (bottom) with the analytical values for various models of grain alignment (left panel) and different viewing angles  $\gamma_{\rm view} = 0^{\circ} - 90^{\circ}$  (right panel). The analytical calculations are well correlated with the synthetic data in all cases of grain alignment and viewing angles.

the grain shape is highly elongated with a large axial ratio s>2.

Figure 25 shows the results of synthetic starlight polarization integral  $\Pi_{\text{syn}}$  calculated from optical-NIR polarization spectrum of background stars generated by the POLARIS code (see Appendix B), assuming both Ideal RAT alignment and Realistic models of PM and SPM grains and  $\gamma_{\text{view}} = 0^{\circ} - 90^{\circ}$ . The values of  $\Pi_{\text{syn}}$ strongly depend on the alignment efficiency, with a significant decrease toward the high-density region of the cloud as a result of the alignment loss by stronger gas randomization. The starlight polarization integral is much lower when grains are paramagnetic and gets increased when grains are superparamagnetic and have higher levels of iron inclusions. Besides, the mean inclination angles of B-fields impact the overall optical-NIR polarization spectrum and the observed starlight polarization integral, leading to a low  $\Pi_{\text{syn}}$  for small  $\gamma_{\text{view}}$ ,

and becomes higher when the mean fields are perpendicular to the LOS (i.e., larger  $\gamma_{\text{view}}$ ).

Figure 26 shows the comparison of the synthetic starlight polarization integral and the analytical one derived from Equation 15 for different alignment models and  $\gamma_{\text{view}} = 90^{\circ}$  (left panel) and various viewing angles (right panel). In all cases, the analytical calculations of starlight polarization integral are in agreement with the synthetic data.

The effect of grain growth is taken into consideration in the numerical calculations of starlight polarization integral, as presented in Figure 27. As the maximum grain size increases up to  $a_{\rm max}=1\,\mu{\rm m}$ , the polarization efficiency integral decreases significantly to  $\Phi(a)<0.4$  (see Figure 24), resulting in the reduction of the synthetic starlight polarization integral  $\Pi_{\rm syn}$  in the whole filamentary cloud.

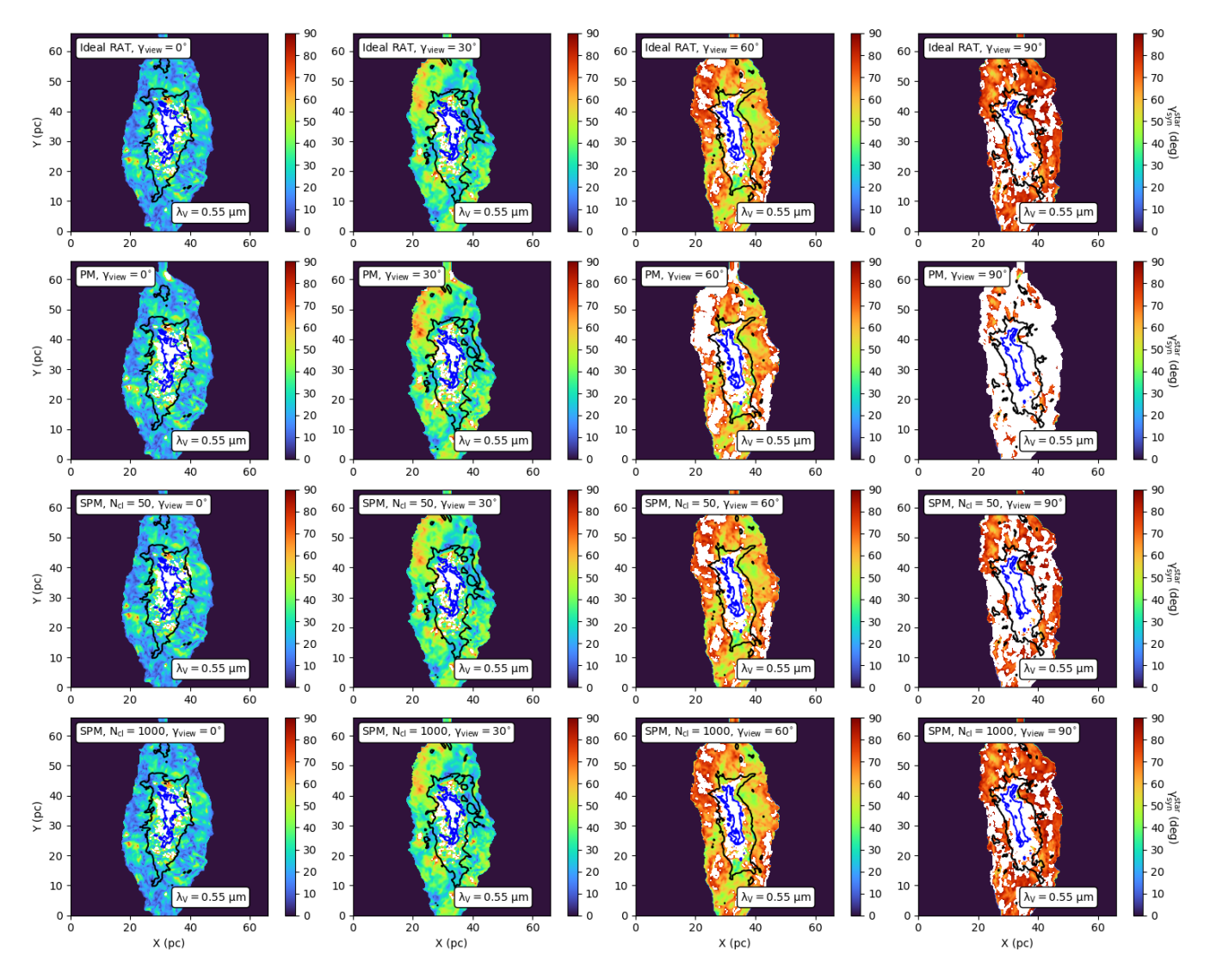


Figure 16. Resulting maps of the inclination angles inferred from the V-band polarization efficiency, assuming both Ideal and Realistic alignment models and the variation of the viewing angle  $\gamma_{\text{view}} = 0^{\circ} - 90^{\circ}$ . The inferred values are independent of both grain alignment models and viewing angles.

# 4.4.2. Inferred inclination angles from starlight polarization integral

Figure 28 shows the maps of inferred inclination angles  $\gamma_{\rm syn}^{\rm spec}$  from the synthetic starlight polarization integral for different alignment models and viewing angles  $\gamma_{\rm view}$ . In comparison with the previous technique using single-band polarization efficiency  $P/N_{\rm H}$  in Figure 16 and 17, the results are independent of the wavelength and can be retrieved up to the densest part of the cloud. Due to the dependence of starlight polarization integral on grain magnetic properties, the results show more NAN values when grains are paramagnetic, and becomes fewer when grains have embedded iron. Besides, the viewing angles and the fluctuation of magnetic fields affect the synthetic starlight polarization integral and the results

of inferred inclination angles, which show fewer NAN values toward the denser region for small  $\gamma_{\rm view}$ .

The distribution of  $\gamma_{\rm syn}^{\rm spec}$  and its probable values for various alignment models and viewing angles are summarized in Figure 29 and Table 4. Similar to the values of inferred inclination angle from the polarization efficiency obtained in Figure 18 and Table 3, the results are less different than the mean values from the MHD simulation as the effect of grain alignment and magnetic turbulence are both considered.

The grain growth effect is included in the calculation of inferred inclination angles from  $\Pi_{\rm syn}$ , which is illustrated in Figure 30. Despite the decreased starlight polarization integral by grain growth, the resulting inferred inclination angles do not change and are the same as the synthetic results in Figure 28.

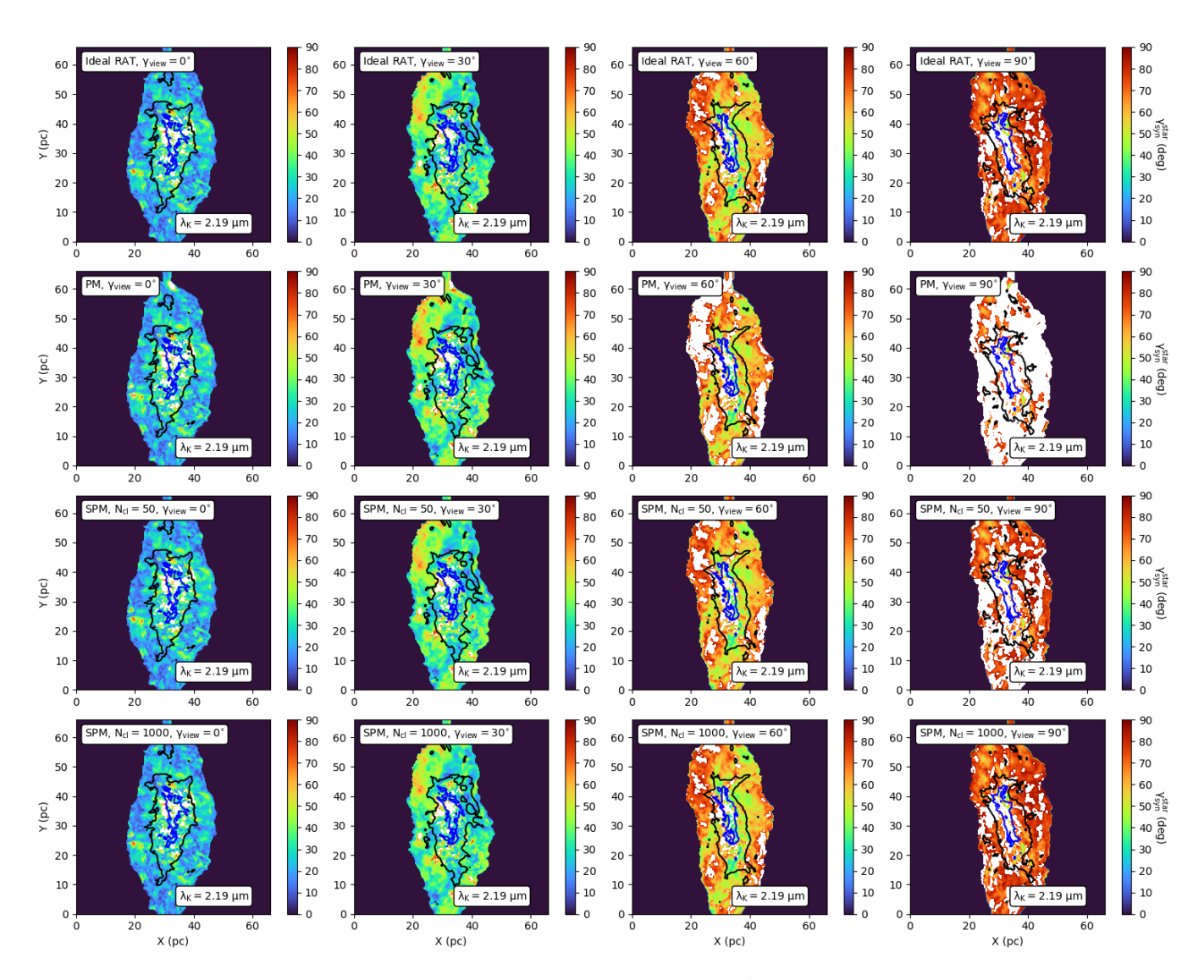


Figure 17. Same as Figure 16 but tracing toward the denser region up to  $A_{\rm V}=30$  when being inferred from the K-band polarization efficiency.

Table 4. Similar to Table 3 but for the inclination angles inferred from the starlight polarization integral  $\Pi_{\text{syn}}$ .

$\gamma_{ m view}$	$\langle \gamma_{ m B}  angle^{ar{\wedge}}$	$\gamma_{ ho}^{ar{\wedge}}$	$\gamma_{ m syn,Ideal\ RAT}^{ m spec}$	$\gamma_{ m syn,MRAT}^{ m spec}$ $(N_{ m cl} = 50)$	$\gamma_{\mathrm{syn,MRAT}}^{\mathrm{spec}^{\bar{\wedge}}}$ $(\mathrm{N_{cl}} = 1000)$
0°	11.36°	29.4°	$25.07^{\circ}$	23.86°	25.43°
$30^{\circ}$	$38.4^{\circ}$	$42.38^{\circ}$	$41.84^{\circ}$	$41.84^{\circ}$	$41.84^{\circ}$
$60^{\circ}$	$67.81^{\circ}$	$60.6^{\circ}$	$62.94^{\circ}$	$64.74^{\circ}$	$62.76^{\circ}$
$90^{\circ}$	$77.01^{\circ}$	$73.04^{\circ}$	$75.75^{\circ}$	$79.72^{\circ}$	$75.75^{\circ}$

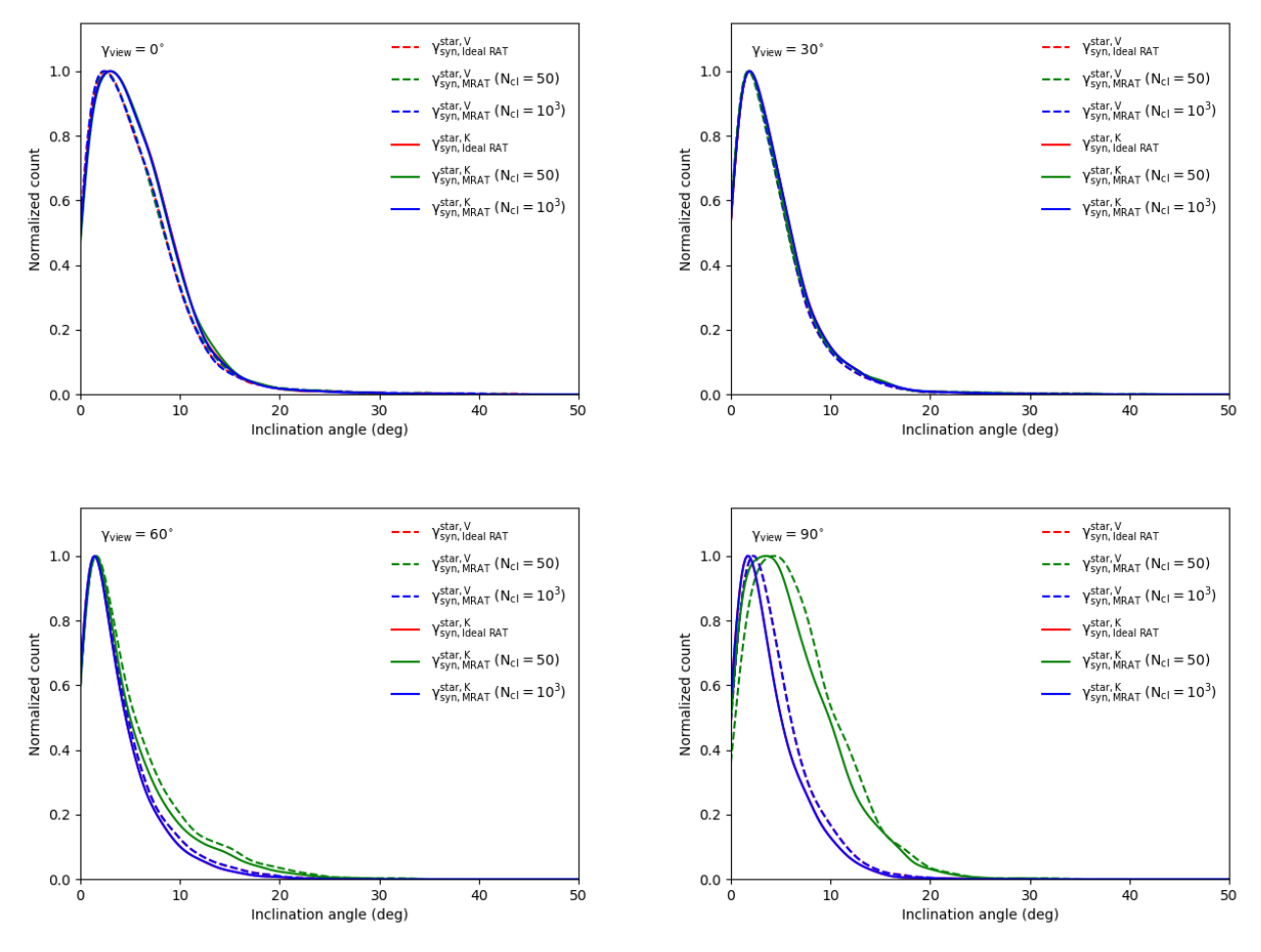


Figure 18. Histogram of the difference between the inferred inclination angles from the polarization efficiency at V-band (dashed color lines) and K-band (solid color lines) with the true mean inclination angles  $\gamma_{\rho}$  for different alignment models and viewing angles. Regardless of grain magnetic properties and viewing angles, our method can accurately retrieve the inclination angles close to the true values from the MHD simulation with the difference of 2 – 6 degrees.

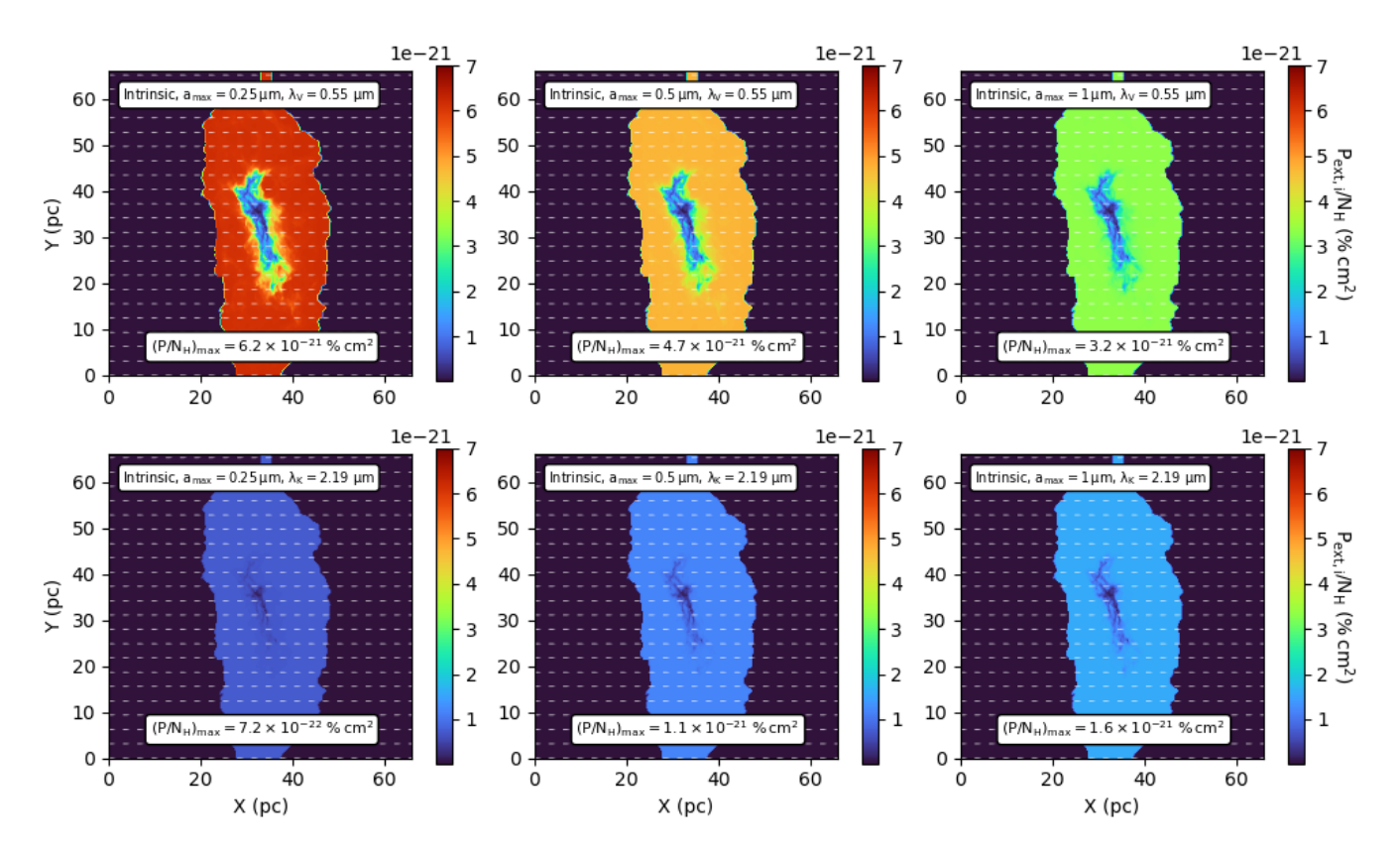


Figure 19. The maps of intrinsic polarization efficiency  $P_{\rm ext,i}/N_{\rm H}$  at V-band (top) and K-band (bottom) when the maximum grain size increases from  $a_{\rm max}=0.25\,\mu{\rm m}$  to  $a_{\rm max}=1\,\mu{\rm m}$ . The V-band polarization efficiency decreases while it increases at the K-band as  $a_{\rm max}$  increases.

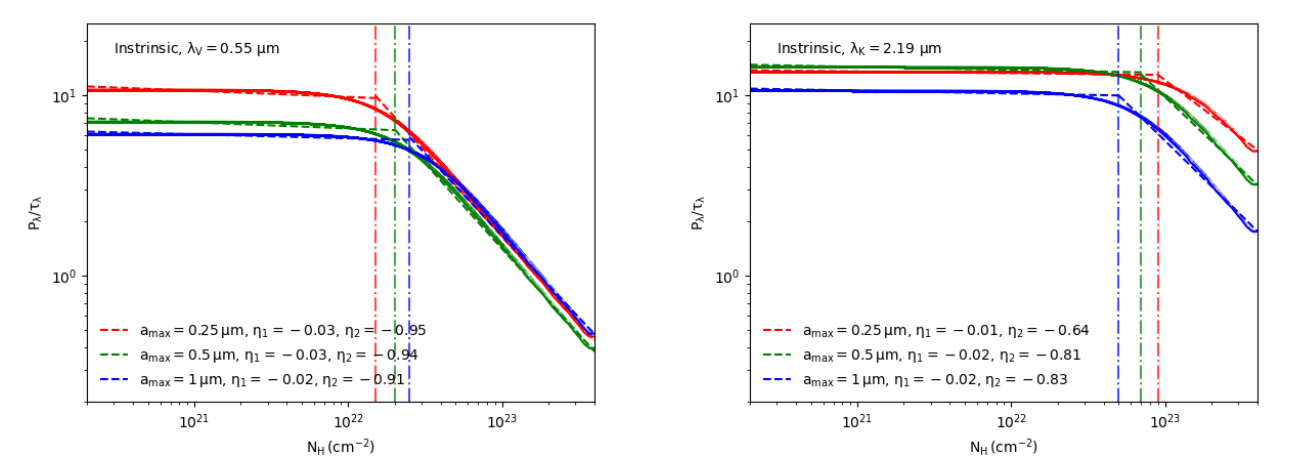


Figure 20. The effect of grain growth on the V-band (left panel) and K-band (right panel) fractional polarization  $P_{\lambda}/\tau_{\lambda}$  with respect to the gas column density  $N_{\rm H}$ . The increasing grain sizes contribute to the decrease in the transition column density  $N_{\rm H,trans}$  for the loss of K-band fractional polarization by the extinction effect, while it increases for V-band fractional polarization.

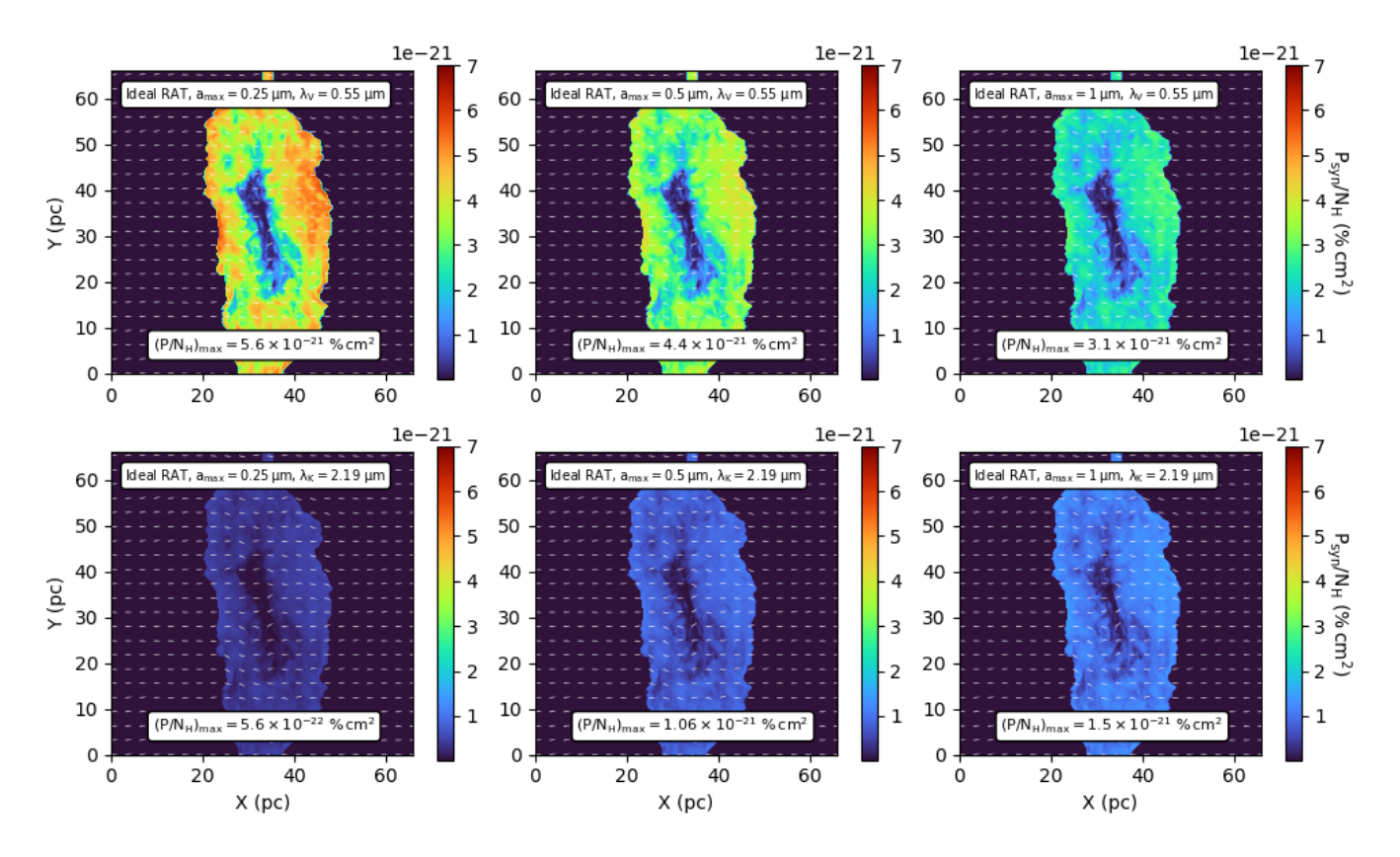


Figure 21. Similar to Figure 19 but for the synthetic polarization efficiency  $P_{\text{syn}}/N_{\text{H}}$  when the grain growth effect and the Ideal RAT alignment are considered.

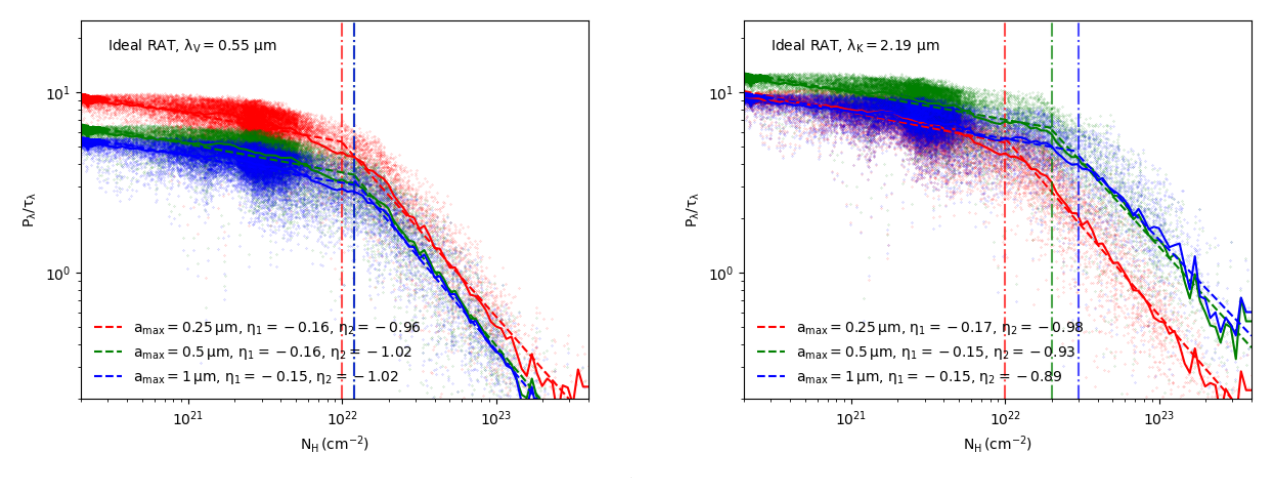


Figure 22. Same as Figure 20 but considering the Ideal RAT alignment case. The alignment of larger grains  $a > 0.25 \,\mu\text{m}$  is enhanced as  $a_{\text{max}}$  increases, leading to the increased transition column density for grain alignment loss to the inner dense cloud.

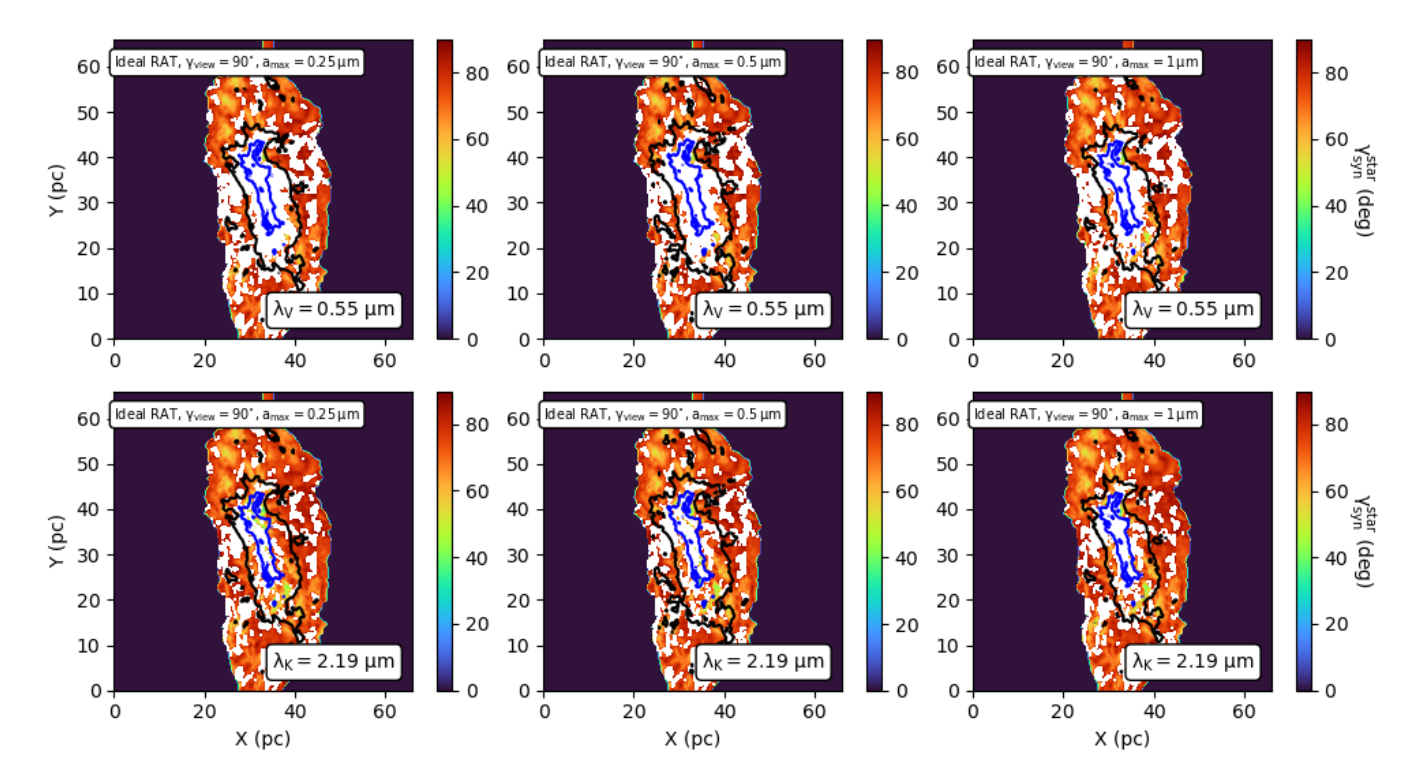


Figure 23. The resulting maps of inferred inclination angles from the V-band and K-band polarization efficiency for increasing  $a_{\text{max}} = 0.25 - 1 \,\mu\text{m}$ . The values of  $\gamma_{\text{syn}}$  seem to be unchanged despite the effect of grain growth.

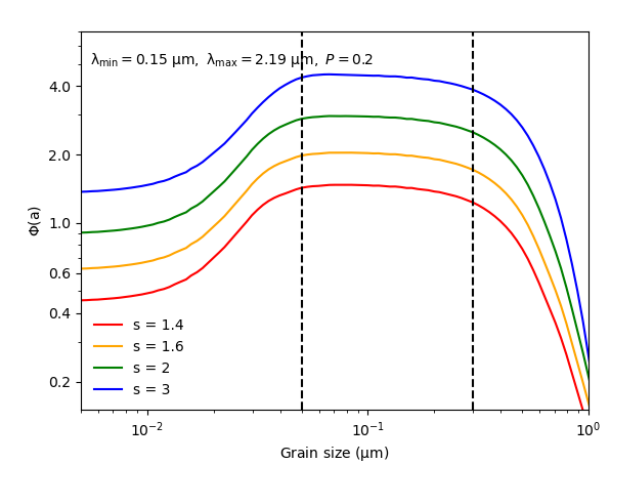


Figure 24. The starlight polarization efficiency integral  $\Phi(a)$  over the wavelengths  $\lambda=0.15-2.19\,\mu\mathrm{m}$  as a function of grain sizes for the model of Astrodust by Draine & Hensley (2021). Different axial ratios s=1.4-3 for oblate grains and the porosity of 20% are assumed. The value of  $\Phi(a)$  increases with increasing grain sizes, and becomes constant at the size range  $a=0.05-0.25\,\mu\mathrm{m}$  highlighted by black dashed lines. For large grains  $a>0.25\,\mu\mathrm{m}$ , the polarization efficiency integral drops to <0.4. The polarization efficiency integral is much higher when grains are highly elongated s>2.

# 5. DISCUSSION

# 5.1. Physical model of starlight polarization based on grain alignment theory

A detailed physical model of absorbed polarization from background stars incorporating modern grain alignment theories and the properties of B-fields' morphology is necessary to investigate its potential of constraining 3D B-fields and dust properties from polarimetric data at optical-NIR wavelengths. In this paper, we introduced the general model of the wavelengthdependent starlight polarization efficiency  $P_{\rm ext}(\lambda)/N_{\rm H}$ as shown in Equation 26 based on (1) the intrinsic polarization efficiency  $P_{\mathrm{ext,i}}(\lambda)/N_{\mathrm{H}}$ , (2) the fraction of polarization efficient  $f_{\rm pol}(\lambda) = \sigma_{\rm pol,alig}/\sigma_{\rm pol}$ , (3) the factor  $F_{\text{turb}}$  describing the levels of magnetic turbulence and (4) the mean inclination angles  $\sin^2 \gamma$ . The intrinsic polarization efficiency  $P_{\mathrm{ext,i}}/N_{\mathrm{H}}$  describes the starlight polarization per H by all grains at wavelength  $\lambda$  in an ideal condition when B-fields are well-ordered and completely in the POS, which then depends only the grain shape. The fraction  $f_{\text{pol}}(\lambda)$  describes the starlight polarization by aligned grains only and strongly depends on the alignment properties  $f_{\text{align}}(a)$  calculated from the MRAT theory for a given environmental condition (e.g., local gas density, radiation intensity, and B-field strength) and grain magnetic properties (e.g., PM or SPM grains with embedded iron) as shown in Equation 17 - 22.

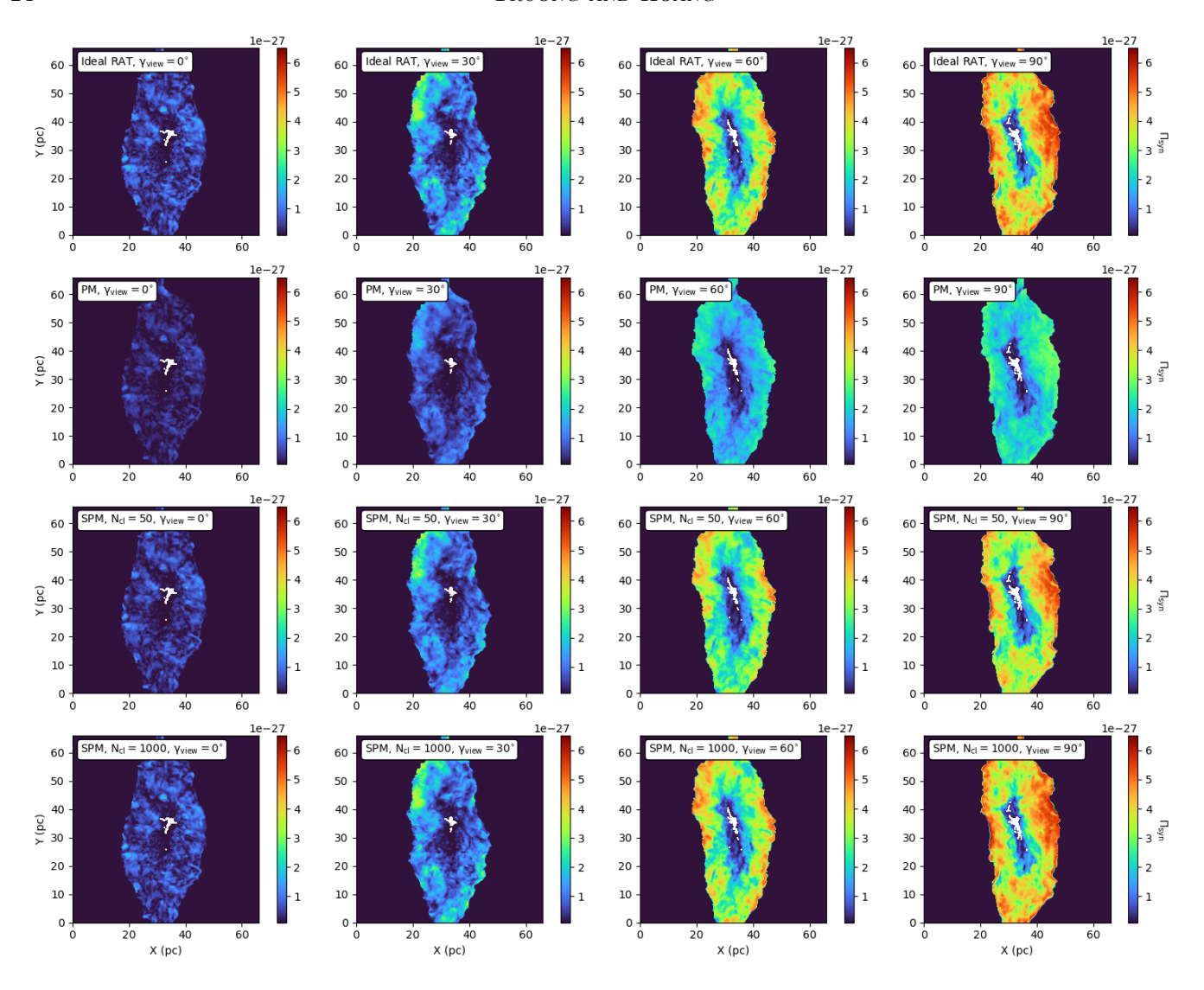


Figure 25. The synthetic starlight polarization integral  $\Pi_{\text{syn}}$  derived from the starlight polarization spectrum at  $\lambda = 0.15 - 2.19 \,\mu m$  for different grain alignment models and viewing angles  $\gamma_{\text{view}} = 0 - 90^{\circ}$ . The integral decreases toward the denser region of the cloud caused by the grain alignment loss. The integral is significantly reduced for PM grains and becomes higher for SPM grains with high levels of iron inclusions. The effect of inclined B-fields also contributes to the decrease in starlight polarization integral for small  $\gamma_{\text{view}}$ .

Our physical model of starlight polarization was quantified and compared with the synthetic starlight polarization efficiency from the background stars behind the filamentary cloud generated by the updated POLARIS code (see the right panel of Figure 9 and Figure 15). Despite the variation with respect to the observed wavelength, the alignment properties, the viewing angle  $\gamma_{\rm view}$ , and the effect of grain growth, our new analytical model well describes the synthetic polarimetric data. This broadens the full capability of starlight polarization in constraining 3D B-fields, grain alignments, and dust properties from single-band polarimetry at optical and NIR wavelengths.

Based on the physical model of starlight polarization, we improved the analytical model of starlight polarization integral  $\Pi_{\rm obs}$  introduced by Draine & Hensley (2021). This parameter is determined by taking the integral over the observed starlight polarization spectrum at optical-NIR wavelengths and depends on both B-fields' properties (e.g., the level of magnetic turbulence  $F_{\rm turb}$  and the mean inclination angles  $\sin^2 \gamma$ ) and grain properties (e.g., the starlight polarization efficiency integral  $\Phi(a)$ , the size distribution  $n_d(a)$  and the alignment degree  $f_{\rm align}(a)$ , see in Equation 15). Here, the dimensionless starlight polarization efficiency  $\Phi(a)$  is used for constraining the intrinsic properties of grains responsible for the starlight polarization, e.g., sizes, shapes, and

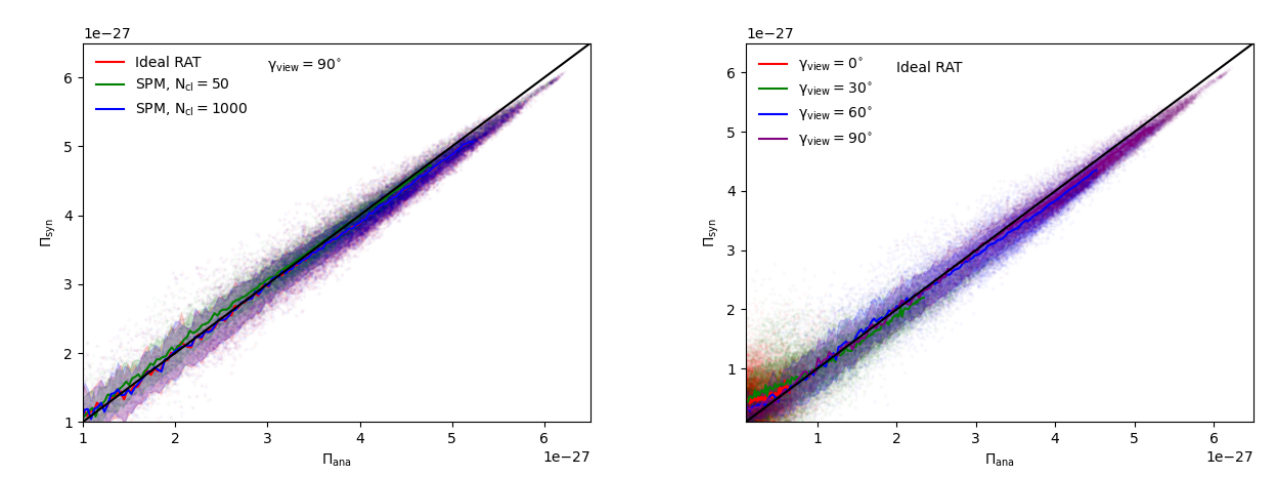


Figure 26. The analytical calculations of the starlight polarization integral  $\Pi_{\rm ana}$  from Equation 15 in comparison with the synthetic data when the variation of grain alignment models (left panel) and viewing angles (right angle) is taken into consideration. The analytical model well describes the synthetic integral taken from the starlight polarization spectrum.

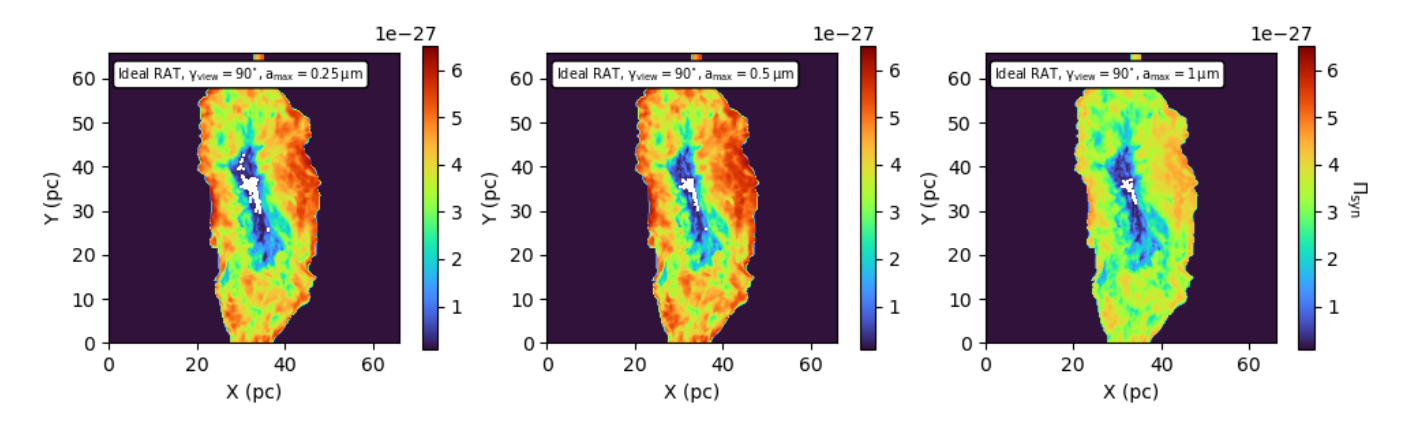


Figure 27. The maps of synthetic starlight polarization integral when the grain growth effect is taken into consideration. The values of  $\Pi_{\text{syn}}$  decreases in the entire cloud with increasing  $a_{\text{max}}$ .

porosities. Our study considers the dependence of  $\Phi(a)$  on both grain elongations and their sizes from nanosized grains  $a=5\,\mathrm{nm}$  to micron-sized grains  $a=1\,\mu\mathrm{m}$ , differing from the constant  $\Phi(a)$  for grains in the diffuse ISM  $a=0.05-0.25\,\mu\mathrm{m}$  in Draine & Hensley (2021) (see the calculation in Figure 24). Consequently, the applications of our new model can be extended in various astrophysical environments, from MCs to dense cores, in which grain growth and grain destruction are commonly taken into consideration. Our analytical calculation of starlight polarization integral is consistent with the one derived from the synthetic starlight polarization spectrum (Figure 26), implying the potential of inferring 3D B-fields and constraining dust properties using multiband polarimetry.

# 5.2. Tracing 3D B-fields in star-forming regions

The studies of 3D B-fields are essential for fully understanding their roles in astrophysical processes in star-forming regions, e.g., the giant filamentary cloud formation (Hennebelle & Inutsuka 2019; Tahani 2022) or the hourglass-shape B-field in magnetized dense cores (Padovani et al. 2012; Basu et al. 2024). The effect of inclined 3D B-fields on the degree of starlight polarization was presented in optical-NIR polarimetric observations of MCs (Lee & Draine 1985; Angarita et al. 2023) and to smaller scales as dense cores (Kandori et al. 2018; Kandori et al. 2020a); however, accurate determination of 3D B-fields from starlight polarization has not been proposed and still challenging.

In this study, we introduced a new technique for tracing 3D B-fields by inferring the inclination angles from the starlight polarization efficiency  $P/N_{\rm H}$  incorporating modern grain alignment theories. We tested with the synthetic polarization from background stars and found

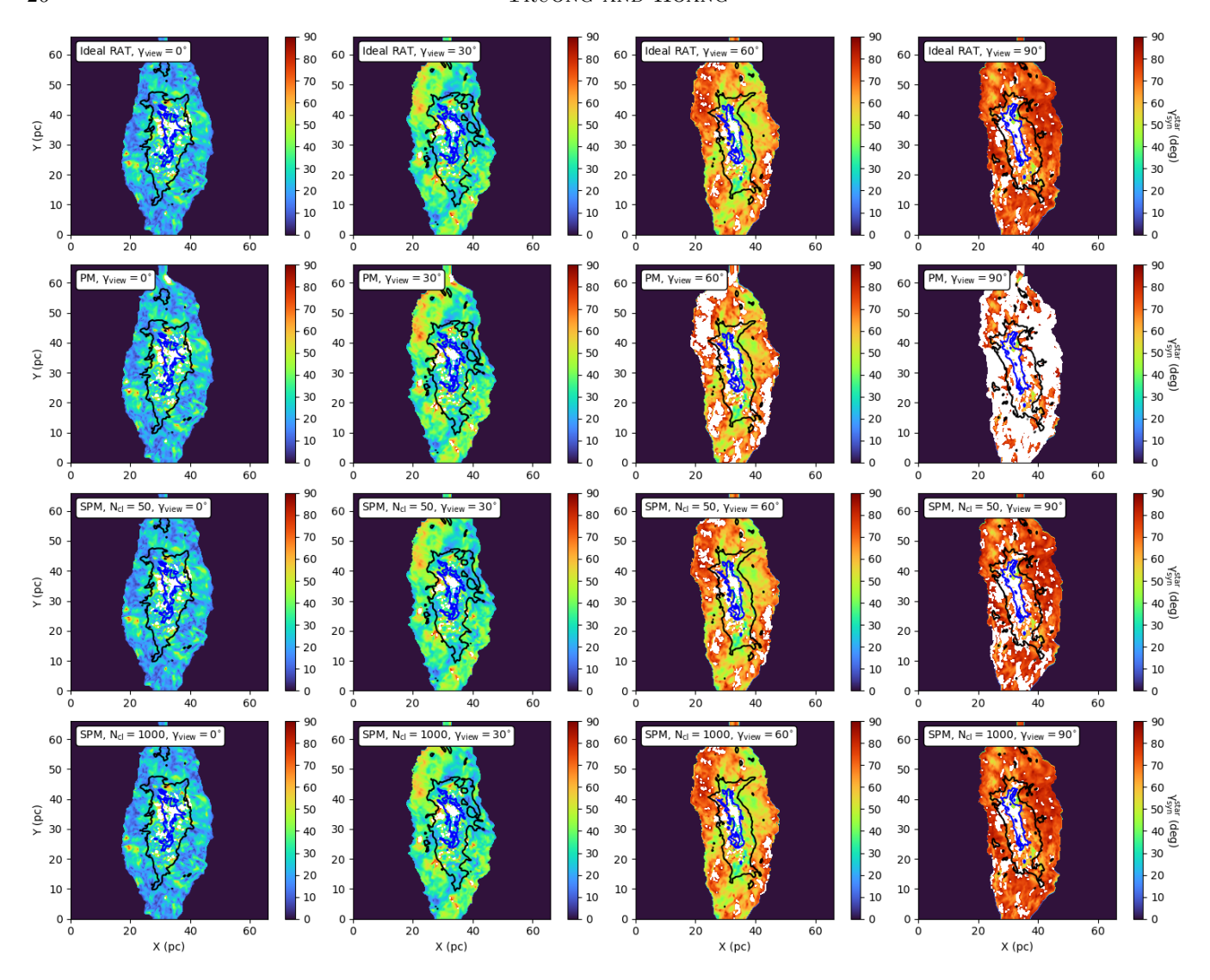


Figure 28. The maps of inferred inclination angles retrieved from the synthetic starlight polarization integral  $\Pi_{\text{syn}}$  for various alignment models and viewing angles. The results are insensitive to the wavelength and could be retrieved to the densest part of the cloud, in comparison with the previous ones using starlight polarization efficiency in Figure 16 and 17.

that the new technique can retrieve the inclination angles from optical polarization only in the low-density region  $N_{\rm H} < 5 \times 10^{21} {\rm cm}^{-2}$  corresponding to  $A_{\rm V} < 3$ , which is applicable in inferring 3D B-fields in the outer region of the giant filamentary clouds (the top panels of Figure 10 and Figure 16). Meanwhile, by using NIR polarization, the local inclination angles can be inferred toward high-density regions up to  $N_{\rm H} \sim 5 \times 10^{22}~{\rm cm}^{-2}$ (i.e.,  $A_{\rm V} \approx 30$ ) where dense filaments/cores are formed and evolved (the bottom panels of Figure 10 and Figure 17). Despite these differences, our new technique provides the local inclination angles close to the true angles derived from MHD simulations by 2-6 degrees (Figure 12) and does not change regardless of grain alignment properties (Figure 18) - similar to what was obtained in the previous technique using thermal dust polarization

degree (Hoang & Truong 2024). Therefore, it is possible to apply the new technique in constraining local 3D B-fields using multi-wavelength polarization on multiple scales of star-forming regions from MCs by optical polarimeters (Panopoulou et al. 2019; Doi et al. 2021; Angarita et al. 2023) to filaments (Chapman et al. 2011; Sugitani et al. 2019; Wang et al. 2020; Chen et al. 2023) and even in dense cores (Kandori et al. 2018; Kandori et al. 2020b) by NIR polarimeters with high sensitivity.

# 5.3. Tracing 3D B-fields in the diffuse ISM

On a large scale of > 1kpc as the diffuse ISM, the presence of 3D B-fields impacts the formation and evolution of multi-phase ISM structures (see the review of Haverkorn 2015). As discussed in the above section, by using our new technique, we can trace the inclination

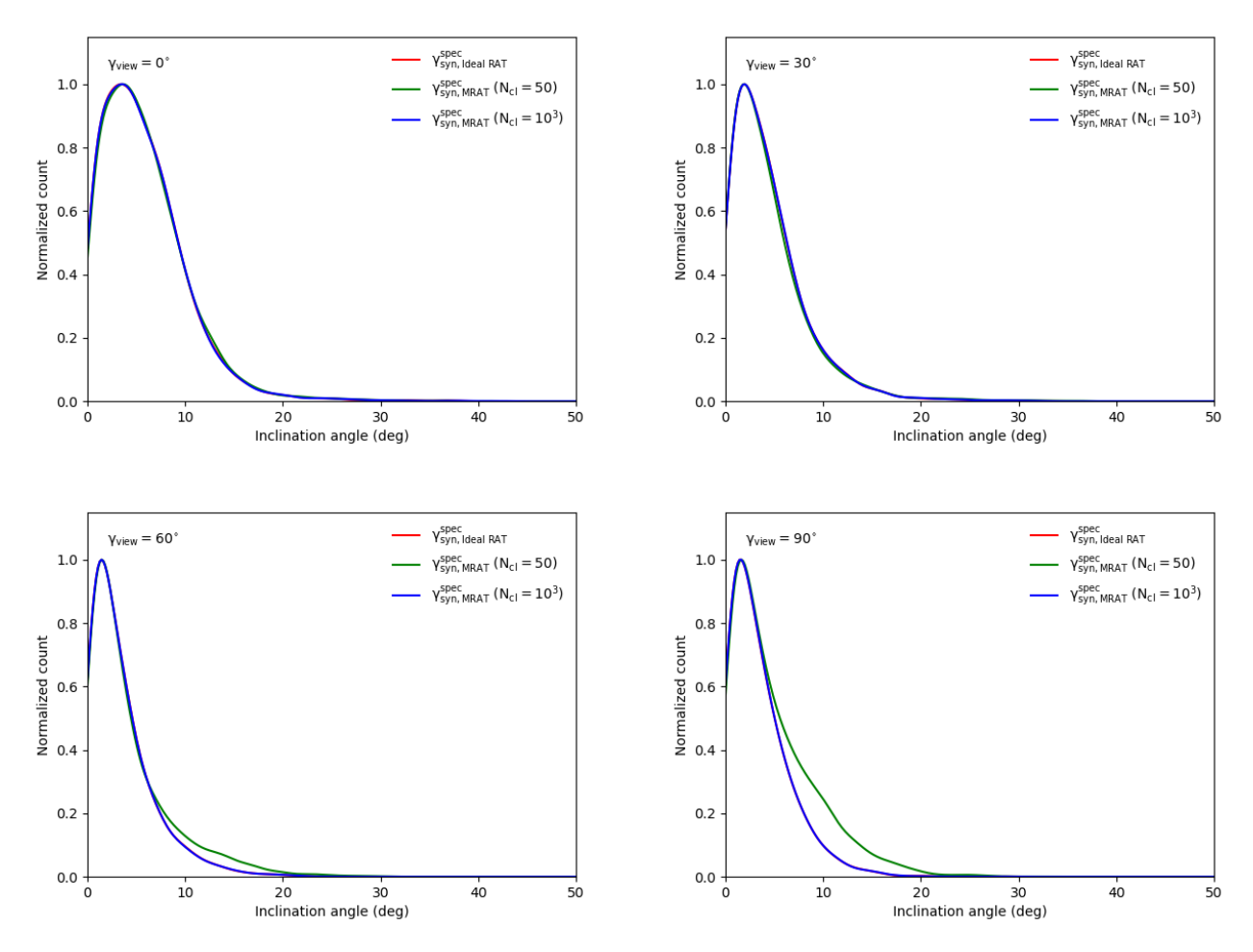


Figure 29. Similar to Figure 18 but for the inclination angles retrieved from the starlight polarization integral. The results are independent of grain alignment models and viewing angles and in better agreement with the true inclination angle from MHD data.

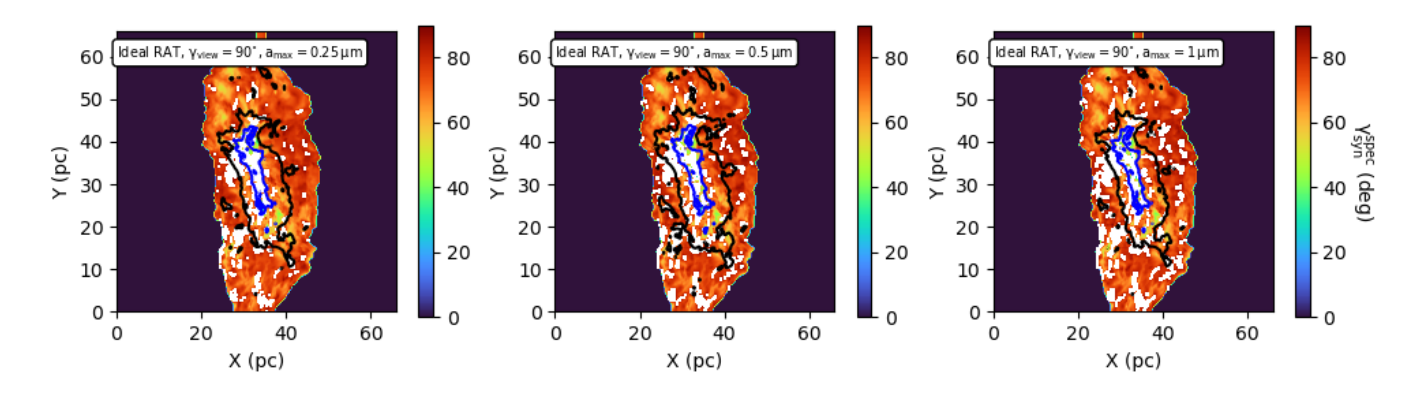


Figure 30. The local inferred inclination angles from the synthetic starlight polarization integral when the grain growth effect is considered. The values of the inclination angle do not change as  $a_{\text{max}}$  increases from  $0.25 \,\mu\text{m}$  to  $1 \,\mu\text{m}$ .

angles from optical starlight polarization efficiency produced by background stars with low-extinction  $A_{\rm V} < 3$  in the magnetized ISM (Figure 10). This can be achievable through modern optical polarization surveys from the Interstellar Polarization Survey in the General ISM (IPS-GI; Versteeg et al. 2023; Angarita et al. 2023) at low- and intermediate-latitude  $|b| < 10^{\circ}$  to the Polar-Areas Stellar Imaging Polarization High Accuracy Experiment (PASIPHAE; Panopoulou et al. 2019) at high-latitude  $|b| > 50^{\circ}$ , providing a full morphology of Galactic B-fields in the three-dimensional space.

Note that the 3D ISM B-fields can be inferred by using the starlight polarization integral  $\Pi_{obs}$  (see Equation 28) for a few samples of background stars with  $A_{\rm V} < 4$ having spectropolarimetric observations from optical to NIR wavelengths (see Chapman et al. 2011; Vaillancourt et al. 2020). Same as the above technique using starlight polarization efficiency, the new method using starlight polarization integral can accurately determine the mean inclination angles, given known dust properties and grain alignment in local environments (Figure 28 and 29). In the case of background stars in the diffuse ISM, the determination of inclination angles from  $\Pi_{\rm obs}$  can be simplified by using  $\Phi(a) \approx \Phi(a_{\rm align})$  and the local mass-weighted alignment efficiency  $\langle f_{\text{align}} \rangle$  (see Equation 33), considering the constraint on grain elongation  $s \gtrsim 1.4$  (see Hensley & Draine 2023). This unlocks a new possibility of constraining both 3D Galactic B-fields, dust properties, and grain alignment physics in the diffuse medium from spectropolarimetric observations.

# 5.4. Applications for 3D B-field topography

The advantage of starlight polarization is that it can reveal the 3D B-fields arising from multiple cloud components along the LOS when the information on the background star's distances is available, whereas polarized thermal emission tells only the average 3D B-field due to the integration effect (see Panopoulou et al. 2019; Pelgrims et al. 2023; Doi et al. 2024). The measurement of B-fields' components along the LOS has been extensively studied with the combination of starlight polarization observations and accurate determination of stellar distances up to a few kpc by the Gaia astrometric mission. The latest study of Doi et al. (2024) separated 2D magnetic field components along the LOS in the Sagittarius Arm using R-band polarization by Hiroshima Optical and Near-InfraRed (HONIR) camera combined with distance measurement in the Gaia Data Release 3 catalog (DR3, Gaia Collaboration et al. 2023). They found the variation of polarization efficiency  $P/A_{\rm V} < 1.4\% \,{\rm mag^{-1}}$  in each isolated cloud component, which could be explained by the effect of Galactic B-fields' inclination angles with respect to the observed POS.

Throughout our study, we have emphasized the applications of our new technique using starlight polarization efficiency to infer the 3D B-fields for multiple clouds along the sightline. Given the polarization efficiency and polarization angle dispersion for each LOS cloud component separated by stellar distances combined with the constrained dust properties and grain alignment physics, we can derive the inclination angles of each LOS magnetic field component (see Appendix C). Due to the sensitive dependence of starlight polarization on the observed wavelength, the application to multi-wavelength will provide the 3D B-fields of the different layers/clouds along the LOS. This contributes to reconstructing the true 3D structures of B-fields from MCs to the diffuse ISM, which is essential for investigating their influences on star formation processes. The complete applications of 3D tomographic imaging of Bfields combined with our new method will be presented in the forthcoming studies.

### 5.5. Applications for constraining dust properties

The polarization of starlight from aligned grains is a powerful tool to constrain dust properties and grain alignment physics in local environments (see the review of Andersson et al. 2015). For instance, the slope  $\alpha$  of  $P/A_{\rm V} \propto A_{\rm V}^{-\alpha}$  at  $A_{\rm V} > 10$  is commonly used for characterizing grain alignment physics in MCs and dense cores with and without embedded protostars (Andersson & Potter 2007; Whittet et al. 2008; Hoang et al. 2021). Meanwhile, the maximum grain size can be constrained by observing the maximum visual extinction  $A_{\text{max,V}}$  where grain alignment still exists, providing evidence of grain growth in dense environments (Hoang et al. 2021). The signature of grain growth can also be detected from the starlight polarization spectrum with large peak wavelengths  $\lambda_{\rm max} > 0.55 \,\mu{\rm m}$  toward highextinction regions  $A_{\rm V} > 4$  (Whittet et al. 2008; Vaillancourt et al. 2020). The observations of the starlight polarization spectrum can also allow the constraint on intrinsic grain properties, e.g., shapes and porosities, through the starlight polarization integral  $\Pi_{\rm obs}$  (see Draine & Hensley 2021; Hensley & Draine 2023). Additionally, Hoang & Lazarian (2016a) have demonstrated the major role of iron inclusions in enhancing dust polarization degree by the MRAT mechanism, especially in dense environments as dense cores and protostars, providing the capability to constrain the levels of embedded iron through both thermal dust polarization and starlight polarization degree.

Our study has demonstrated the importance of dust properties in the precise calculation of inferred inclination angles from starlight polarization efficiency  $P/N_{\rm H}$ and the starlight polarization integral  $\Pi_{\rm obs}$ . Given the constrained dust properties, e.g., intrinsic and magnetic properties (Section 4.3.2, 4.3.4 and Appendix A), we can determine the local inclination angles of the mean fields with high accuracy. Therefore, the potential of constraining 3D B-fields and dust properties using starlight polarization are associated with each other. And vice versa, our physical model of starlight polarization can help constrain the dust properties and grain alignment physics when the information on 3D B-fields is available. This possibility can be done by comparing the inferred inclination angles from our techniques with the available inclination angles derived from other methods, e.g., the combination of dust polarization and Faraday rotation (Tahani et al. 2018; Tahani et al. 2022) or the combination of dust polarization and Zeeman splitting (Reissl et al. 2021), which will be investigated further in the future studies.

### 6. SUMMARY

We have extended our new technique for probing 3D magnetic fields using thermal dust polarization at far-IR/sub-mm and grain alignment theory from Hoang & Truong (2024) to starlight polarization at optical/NIR. Our results are summarized as follows:

- We introduced a physical model of starlight polarization efficiency using the grain alignment theory based on MRAT combined with the effect of magnetic turbulence. At optical/NIR wavelengths, the degree of starlight polarization is a function of the intrinsic polarization, the fraction of polarization coefficient from aligned grains induced by MRAT, the magnetic fluctuation effect, and the B-field inclination angles.
- 2. We tested our physical polarization model by performing synthetic starlight polarization observations of MHD simulations for a filamentary cloud using the upgraded POLARIS code. We found that the physical polarization model can accurately describe the synthetic absorbed polarization from background stars.
- 3. Using our tested physical polarization model and synthetic polarization data, we inferred the inclination angles of the mean 3D B-fields. Using optical starlight polarization, the inclination

- angles can only be inferred in low-density regions  $N_{\rm H} < 5 \times 10^{21}~{\rm cm}^{-2}$  (i.e.,  $A_{\rm V} < 3$ ), while they can be inferred toward high-density regions up to  $5 \times 10^{22}~{\rm cm}^{-2}$  (i.e.,  $A_{\rm V} \approx 30$ ) when using NIR polarization. Despite the dependence on the observed wavelength, grain properties, B-fields' properties, and alignment physics, our new method provides an accurate inference of inclination angle close to the actual values from MHD simulations by 2-6 degrees.
- 4. Our new method can be applied to real observation data to constrain 3D B-fields using multiwavelength starlight polarization data in multiscale star-forming regions, from large scales as the diffuse ISM/molecular clouds with  $A_{\rm V} < 3$  at optical wavelengths to small scales as dense filaments/cores with  $A_{\rm V} \sim 8-30$  at NIR wavelengths.
- 5. Our new method can be applied to determine the B-field inclination angles from multiple cloud components along the line-of-sight, providing tomographic imaging of true Galactic 3D B-fields using multi-wavelength polarization data combined with the precise determination of stellar distances.
- 6. We also introduced a new technique of inferring inclination angles using starlight polarization integral  $\Pi_{\rm obs}$  derived from the starlight polarization spectrum incorporating grain intrinsic properties (i.e., sizes and shapes) and modern MRAT alignment theory. The new technique can provide an accurate measurement of the inclination angles and the 3D magnetic fields. Our new method can potentially be applied in constraining both dust properties and 3D B-fields using available spectropolarimetric data of low-extinction background stars  $A_{\rm V} < 4$  in the diffuse ISM.
- 7. When the information of 3D B-fields is provided, our physical model of starlight polarization can help constrain the dust properties, such as the grain elongation and magnetic properties, and grain alignment physics.

# ACKNOWLEDGMENTS

T.H. is supported by the National Research Foundation of Korea (NRF) grant funded by the Korean government (MSIT (No. 2019R1A2C1087045). This work was partly supported by a grant from the Simons Foundation to IFIRSE, ICISE (916424, N.H.).

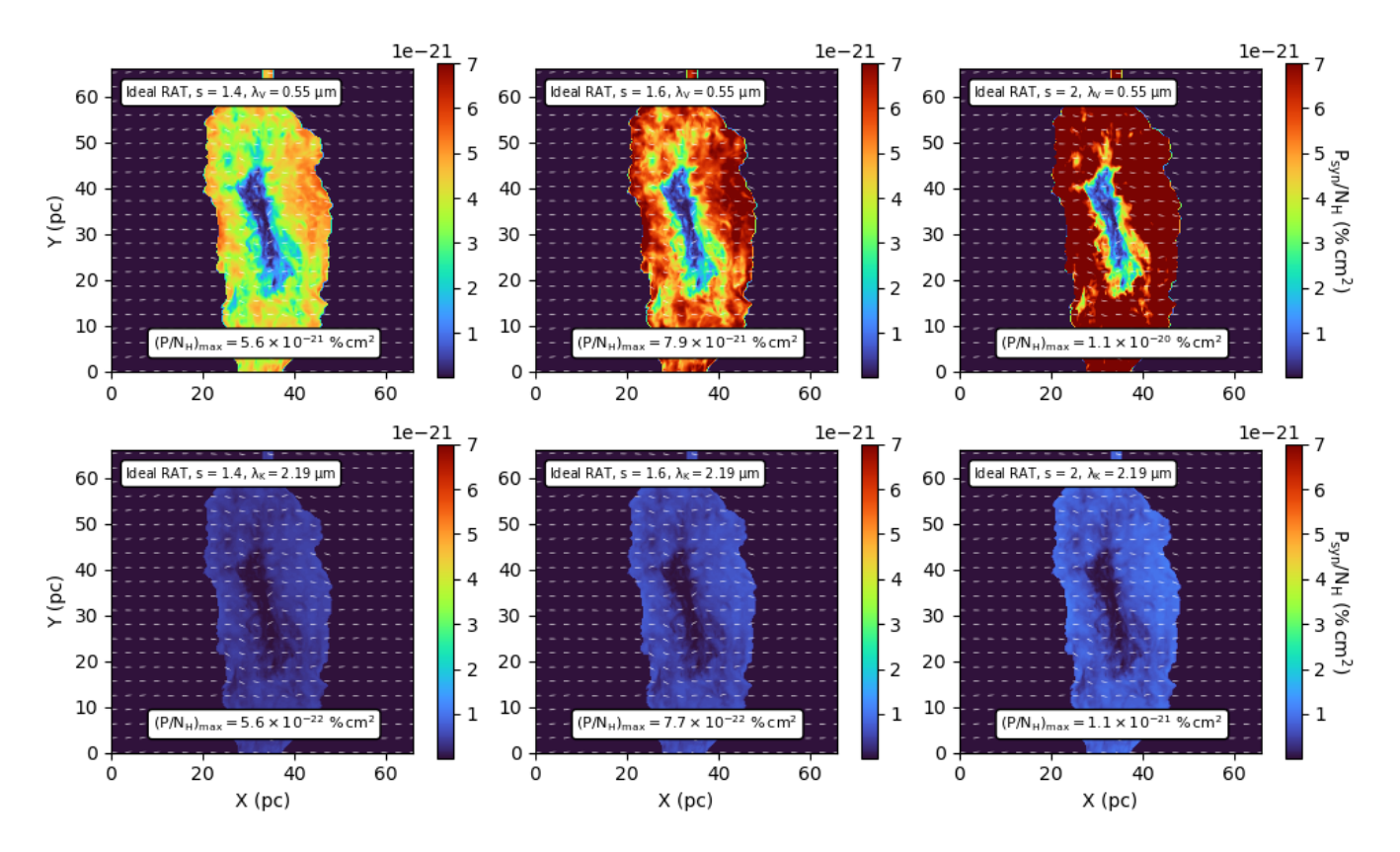


Figure 31. The resulting V-band (top panels) and K-band (bottom panels) starlight polarization efficiency  $P/N_{\rm H}$  for different axial ratios s=1.4-2. As grains become highly elongated to s=2, the polarization efficiency in the entire filamentary cloud increases by a factor of  $\sim 2$ .

# APPENDIX

# A. EFFECT OF GRAIN ELONGATION ON THE CALCULATIONS OF INFERRED INCLINATION ANGLES FROM STARLIGHT POLARIZATION

In this section, we present the impact of grain elongation on the calculations of inferred inclination angles from starlight polarization. We take the Astrodust model of oblate grains by Draine & Hensley (2021) for different axial ratios from s=1.4 (less elongated) to s=2 (highly elongated). We quantify their main effect on the synthetic starlight polarization efficiency  $P/N_{\rm H}$  and the inferred inclination angles  $\gamma_{\rm syn}^{\rm star}$ .

Figure 31 shows the V-band (top) and K-band (bottom) starlight polarization efficiency  $P_{\text{syn}}/N_{\text{H}}$  for increasing axial ratios s, while Figure 32 illustrates the inclination angles inferred from the above polarization efficiency. One can obtain that the polarization efficiency at all observed wavelengths increases by a factor of 2 as grains become highly elongated (i.e.,  $s \approx 2$ ). In spite of these differences with respect to grain elongation, the inferred inclination angles do not change and are comparable to the results in Figure 16 and 17. This emphasizes the applications of our new technique in inferring 3D B-fields using starlight polarization to arbitrary grain shapes.

### B. SYNTHETIC STARLIGHT POLARIZATION SPECTRUM

Figure 33 presents the synthetic polarization spectrum at  $\lambda=0.1-7\,\mu\mathrm{m}$  for background stars located in the outer region (i.e.,  $N_{\mathrm{H}}=7\times10^{21}~\mathrm{cm^{-2}}$ , left panel) and inner region (i.e.,  $N_{\mathrm{H}}=6\times10^{22}~\mathrm{cm^{-2}}$ , right panel) of the filamentary cloud. Both Ideal and Realistic alignment models,  $a_{\mathrm{max}}=0.25\,\mu\mathrm{m}$  and the viewing angle  $\gamma_{\mathrm{view}}=90^{\circ}$  are considered. In general, the wavelength-dependent polarization efficiency becomes lower, and the peak spectrum is shifted to longer wavelengths  $\lambda\sim0.4-0.5\,\mu\mathrm{m}$  in the denser region where grain alignment loss is more efficient. The overall polarization spectrum can be much lower for PM grains, and increase significantly as grains have iron inclusion  $N_{\mathrm{cl}}>50$ .

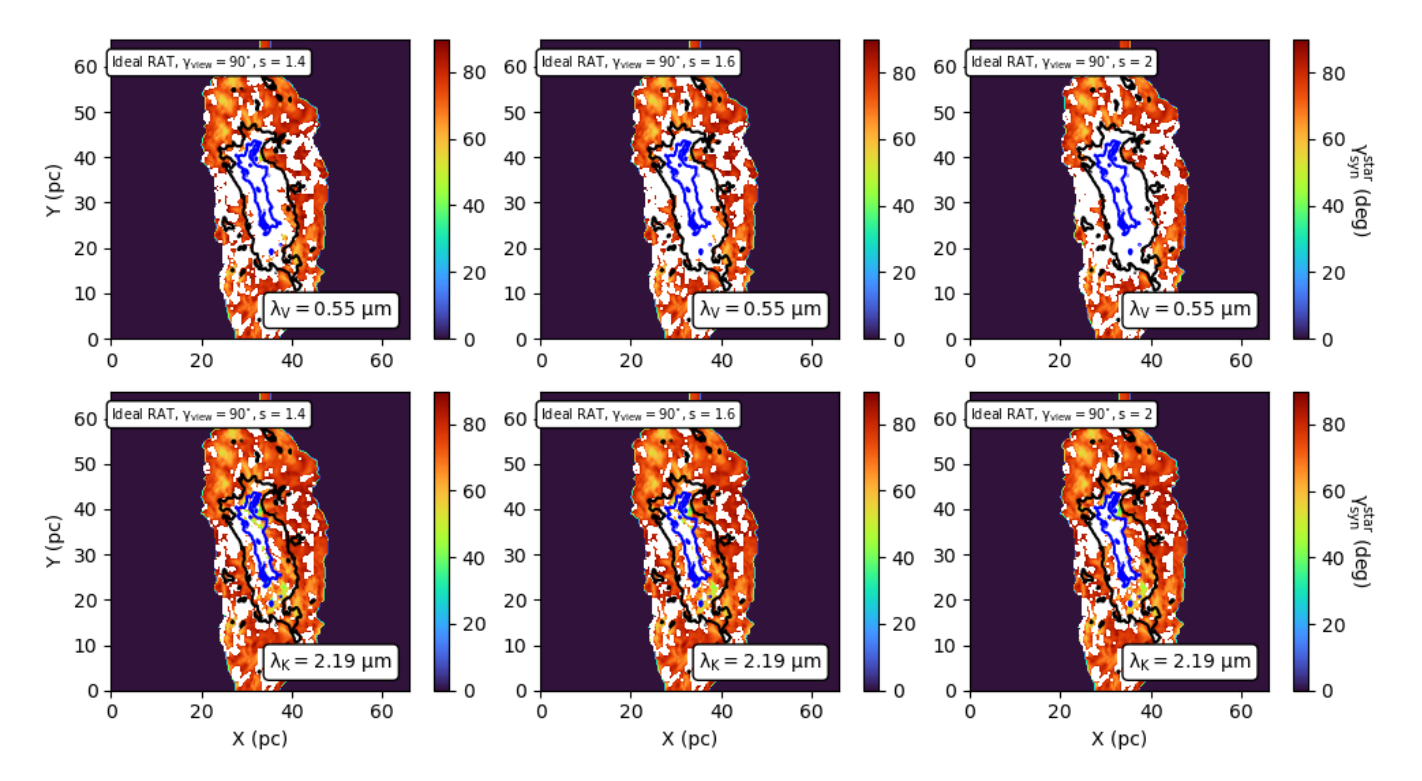


Figure 32. The inferred inclination angles from starlight polarization efficiency at V-band (top panels) and K-band (bottom panels), but considering the variation of grain elongation. The values of  $\gamma_{\text{syn}}^{\text{star}}$  are unchanged in comparison to the results in Figure 16 and 17.

Figure 34 shows the effect of viewing angles  $\gamma_{\text{view}}$  on the starlight polarization spectrum observed in the outer and inner regions. The polarization spectrum is significantly low due to the projection effect of the inclined mean B-fields on the POS for small  $\gamma_{\text{view}}$ , and becomes higher with increasing  $\gamma_{\text{view}}$  (i.e.,  $\sin^2 \gamma \sim 1$ ).

The impact of grain growth on the starlight polarization spectrum is presented in Figure 35 with increasing maximum grain sizes  $a_{\rm max} = 0.25 - 1\,\mu{\rm m}$ . The polarization spectrum gets decreased at optical wavelengths  $\lambda = 0.1 - 0.8\,\mu{\rm m}$ , while it gets increased at NIR wavelengths  $\lambda > 1\,\mu{\rm m}$  - similar to what was obtained in the polarization efficiency maps at V-band and K-band in Figure 21. In the inner dense region  $N_{\rm H} = 6 \times 10^{22}~{\rm cm}^{-2}$ , the spectrum is shifted toward NIR regimes with the peak wavelength of  $\lambda_{\rm max} \sim 1 - 2\,\mu{\rm m}$  produced by the alignment of larger grains  $a > 0.25\,\mu{\rm m}$  enhanced by grain growth.

# C. APPLICATIONS TO OBSERVATIONAL DATA

So far, we have applied our new technique to synthetic data to infer 3D B-fields using starlight polarization. In this section, we present the following steps for applying the new technique to real polarimetric data from observed background stars at optical-NIR bands.

- 1. We first constrain the grain properties (e.g., size distribution and elongation) to be used for calculations of the intrinsic polarization efficiency  $P_{\rm ext,i}/N_{\rm H}$  within the cloud of interest. The grain elongation can be constrained by fitting the observed maximum starlight polarization efficiency at optical/NIR with the modeled one in which the magnetic field is lying in the POS (i.e.,  $\sin^2 \gamma = 1$ ), well-ordered (i.e.,  $F_{\rm turb} = 1$ ) and Ideal RAT alignment (i.e., R = 1) as  $(P_{\rm ext}/N_{\rm H})_{\rm max} \approx (P_{\rm mod}/N_{\rm H})_{\rm max}$  (see Hensley & Draine 2023), whereas the grain size distribution can be constrained by the dust opacity spectral index  $\beta$  of thermal dust emission at far-IR/sub-mm (see Draine 2006; Kwon et al. 2009).
- 2. Derive the volume number gas density  $n_{\rm H}$  from the column density  $N_{\rm H}$  along the LOS as  $N_{\rm H} = \int_{\rm LOS} n_{\rm H} {\rm ds}$  and the radiation field from dust temperature in the local environments.

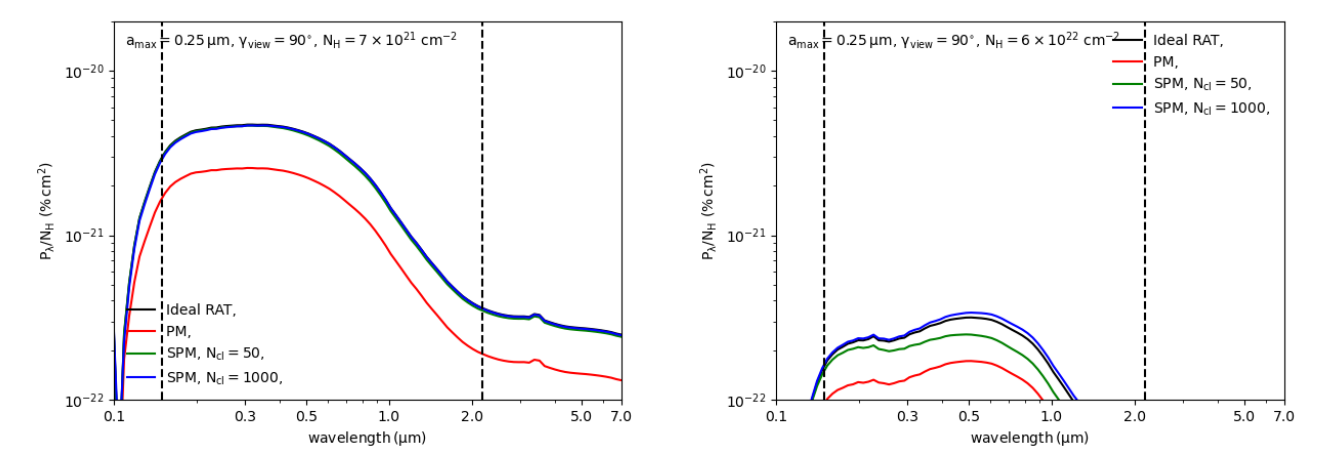
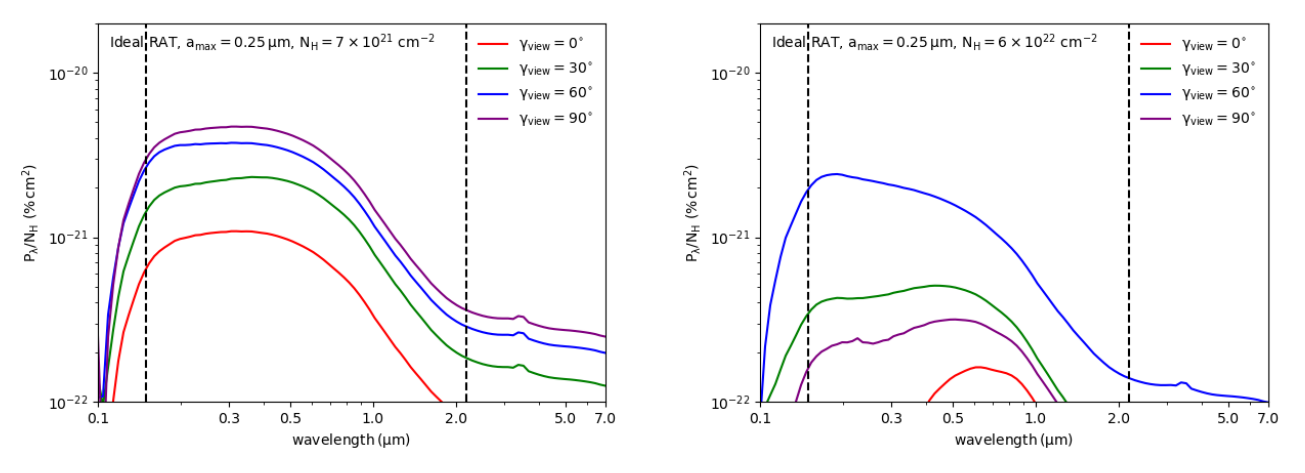


Figure 33. The synthetic optical-NIR polarization spectrum from background stars located at the outer part (i.e.,  $N_{\rm H}=7\times10^{21}~{\rm cm^{-2}}$ , left panel) and the inner part of the cloud (i.e.,  $N_{\rm H}=6\times10^{22}~{\rm cm^{-2}}$ , right panel). Black dashed lines show  $\lambda_{\rm min}=0.15\,\mu{\rm m}$  and  $\lambda_{\rm max}=2.19\,\mu{\rm m}$  for the calculation of  $\Pi_{\rm syn}$ . Both Ideal and Realistic alignment models for PM and SPM grains with  $N_{\rm cl}=50-1000$  are being assumed. The peak of the polarization spectrum shifts to longer wavelengths  $\lambda\sim0.5\,\mu{\rm m}$  produced by aligned large grains in the denser cloud. The polarization efficiency is higher in all wavelengths as grains have high levels of embedded iron.



**Figure 34.** Similar to Figure 33 but for various viewing angles and the Ideal RAT alignment model. The polarization efficiency is reduced in all optical-NIR wavelengths when  $\gamma_{\text{view}}$  is smaller.

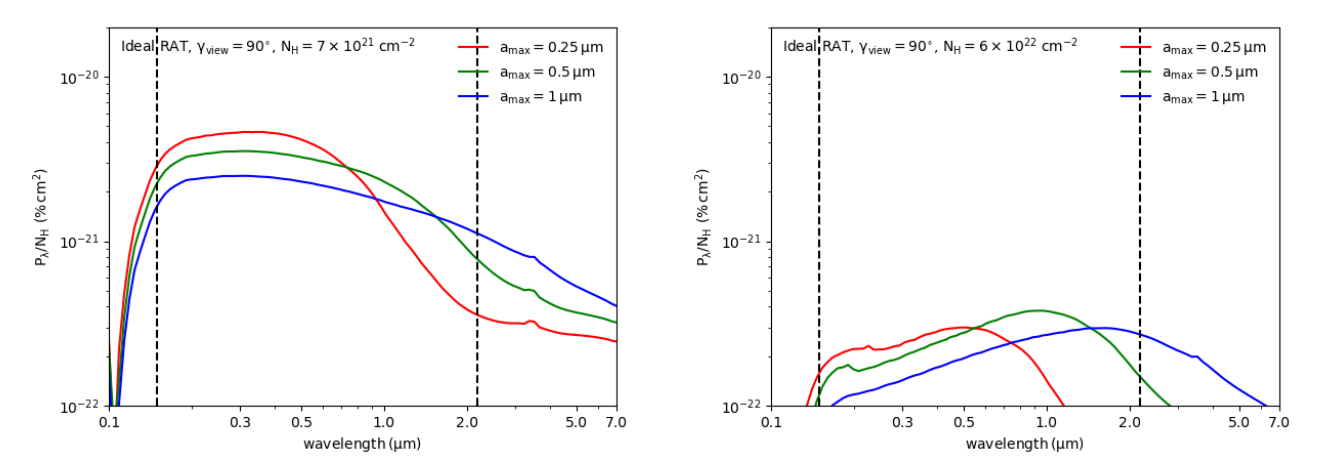


Figure 35. Same as Figure 33 but considering increasing maximum grain sizes from  $0.25\mu m$  to  $1 \mu m$ . The polarization efficiency increases significantly at NIR wavelengths with the spectrum peak at  $\lambda \sim 1 - 2 \mu m$  in the denser part of the cloud as  $a_{\rm max}$  increases.

- 3. Derive the polarization angular dispersion ( $\delta\phi$ ) and the turbulence velocity dispersion from the velocity gas profile ( $\delta v$ ) to apply the DCF method to calculate the B-field strength,  $B_{POS}$  (see in Chapman et al. 2011).
- 4. Calculate the minimum grain alignment size  $a_{\text{align}}$  from Equation 17, the magnetic relaxation  $\delta_m$  from Equation 20 and the alignment degree  $f_{\text{align}}(a)$  for given magnetic properties of grains (e.g., PM or SPM grains with  $N_{\text{cl}}$ ) from Equation 22 (see also Figure 2). Combined with the polarization cross-section  $C_{\text{pol}}(a,\lambda)$  from the constrained size distribution and shape, the fraction of polarization coefficient  $f_{\text{pol}}(\lambda)$  can be computed as presented in Equation 25.
- 5. Calculate  $F_{\text{turb}}$  using the polarization angle dispersion of  $\delta \phi$  (see the analysis of  $F_{\text{turb}}$  in Appendix B in Hoang & Truong 2024)
- 6. With  $P_{\text{ext,i}}/N_{\text{H}}$ ,  $f_{\text{pol}}$ ,  $F_{\text{turb}}$ , and  $P_{\text{ext}}/N_{\text{H}}$  available at a certain polarimetric band, the local B-field inclination angles are inferred using Equation 27.

Note that this technique can be applicable to trace 3D B-fields in the diffuse ISM and nearby star-forming regions from the ratio of observed polarization to visual extinction  $P_{\lambda}/A_{\rm V}$  as  $N_{\rm H}/A_{\rm V}\approx 1.87\times 10^{21}\,{\rm H\,cm^{-2}mag^{-1}}$ , or from the ratio of observed polarization to reddening  $P_{\lambda}/E(B-V)$  as  $N_{\rm H}/E(B-V)\approx 5.8\times 10^{21}\,{\rm cm^{-2}mag^{-1}}$  in the averaged Galactic line-of-sight (Bohlin et al. 1978). For multiple layers/clouds along the LOS, the 3D B-fields can be retrieved from the  $P_{\lambda}/A_{\rm V}$  at each cloud component, where  $A_{\rm V}$  is precisely determined over stellar distances from Gaia astrometric mission (see Zucker et al. 2021; Angarita et al. 2023). We will apply this technique to interpret the 3D B-fields morphologies in multi-scale star-forming regions, or in multiple layers/clouds along the sightline in the ISM using multi-wavelength polarimetric data in the following studies.

# REFERENCES

Andersson, B.-G., Lazarian, A., & Vaillancourt, J. E. 2015, ARA&A, 53, 501

Andersson, B.-G., & Potter, S. B. 2007, ApJ, 665, 369

Angarita, Y., Versteeg, M. J. F., Haverkorn, M., et al. 2023, The Astronomical Journal, 166, 34

Basu, S., Li, X., & Bino, G. 2024, Universe, 10, 218

Bohlin, R. C., Savage, B. D., & Drake, J. F. 1978, ApJ, 224, 132

Chandrasekhar, S., & Fermi, E. 1953, ApJ, 118, 113

Chapman, N. L., Goldsmith, P. F., Pineda, J. L., Li, D., & Krčo, M. 2011, ApJ, 741, 21

Chen, Z., Sefako, R., Yang, Y., et al. 2023, MNRAS, 525, 107

Clemens, D. P., Tassis, K., & Goldsmith, P. F. 2016, ApJ, 833, 176

Clemens, D. P., Cashman, L. R., Cerny, C., et al. 2020, ApJS, 249, 23

Crutcher, R. M. 2010, Highlights of Astronomy, 15, 438

Davis, L. 1951, Physical Review, 81, 890

Davis, L. J., & Greenstein, J. L. 1951, ApJ, 114, 206

Doi, Y., Hasegawa, T., Bastien, P., et al. 2021, The Astrophysical Journal, 914, 122

Doi, Y., Nakamura, K., Kawabata, K. S., et al. 2024, ApJ, 961, 13

Dolginov, A. Z., & Mitrofanov, I. G. 1976, (Astronomicheskii Zhurnal, 19, 758) Draine, B. T. 2006, ApJ, 636, 1114

Draine, B. T., & Hensley, B. S. 2021, The Astrophysical Journal, 919, 65

Draine, B. T., & Weingartner, J. C. 1996, ApJ, 470, 551

Draine, B. T., & Weingartner, J. C. 1997, ApJ, 480, 633

Gaia Collaboration, Vallenari, A., Brown, A. G. A., et al. 2023, A&A, 674, A1

Giang, N. C., Hoang, T., Kim, J.-G., & Tram, L. N. 2023, Monthly Notices of the Royal Astronomical Society, 520, 3788

Goodman, A. A., Bastien, P., Menard, F., & Myers, P. C. 1990, ApJ, 359, 363

Goodman, A. A., Jones, T. J., Lada, E. A., & Myers, P. C. 1995, ApJ, 448, 748

Greenberg, J. M. 1968, in Nebulae and Interstellar Matter, ed. B. M. Middlehurst & L. H. Aller, 221

Hall, J. S. 1949, Science, 109, 166

Haverkorn, M. 2015, in Astrophysics and Space Science Library, Vol. 407, Magnetic Fields in Diffuse Media, ed. A. Lazarian, E. M. de Gouveia Dal Pino, & C. Melioli, 483

Heiles, C. 2000, AJ, 119, 923

Hennebelle, P., & Inutsuka, S.-i. 2019, Frontiers in Astronomy and Space Sciences, 6, 5

Hensley, B. S., & Draine, B. T. 2021, The Astrophysical Journal, 906, 0

- Hensley, B. S., & Draine, B. T. 2023, The Astrophysical Journal, 948, 55
- Hiltner, W. A. 1949, Nature, 163, 283
- Hoang, T., & Lazarian, A. 2008, MNRAS, 388, 117
- Hoang, T., & Lazarian, A. 2014, MNRAS, 438, 680
- Hoang, T., & Lazarian, A. 2016a, ApJ, 831, 159
- Hoang, T., & Lazarian, A. 2016b, ApJ, 821, 91
- Hoang, T., Tram, L. N., Lee, H., Diep, P. N., & Ngoc, N. B. 2021, ApJ, 908, 218
- Hoang, T., & Truong, B. 2024, The Astrophysical Journal, 965, 183
- Hoang, T., Vinh, N. A., & Quynh Lan, N. 2016, ApJ, 824, 18
- Jones, R. V., & Spitzer, L. 1967, ApJ, 147, 943
- Jones, T. J. 1989, ApJ, 346, 728
- Jones, T. J., Klebe, D., & Dickey, J. M. 1992, ApJ, 389, 602
- Kandori, R., Nagata, T., Tazaki, R., et al. 2018, ApJ, 868, 94
- Kandori, R., Tomisaka, K., Saito, M., et al. 2020a, ApJ, 888, 120
- Kandori, R., Tomisaka, K., Saito, M., et al. 2020b, ApJ, 888, 120
- Kwon, W., Looney, L. W., Mundy, L. G., Chiang, H.-F., & Kemball, A. J. 2009, ApJ, 696, 841
- Lazarian, A., & Hoang, T. 2007, MNRAS, 378, 910
- Lazarian, A., & Hoang, T. 2008, ApJ, 676, L25
- Lee, H., Hoang, T., Le, N., & Cho, J. 2020, ApJ, 896, 44
- Lee, H. M., & Draine, B. T. 1985, Astrophysical Journal, 290, 211
- Mathis, J. S., Mezger, P. G., & Panagia, N. 1983, A&A, 128, 212
- Mathis, J. S., Rumpl, W., & Nordsieck, K. H. 1977, ApJ, 217, 425
- Ntormousi, E., & Hennebelle, P. 2019, Astronomy & Astrophysics, 625, A82

- Padovani, M., Brinch, C., Girart, J. M., et al. 2012, A&A, 543, 16
- Panopoulou, G. V., Tassis, K., Skalidis, R., et al. 2019, The Astrophysical Journal, 872, 56
- Pelgrims, V., Panopoulou, G. V., Tassis, K., et al. 2023, Astronomy & Astrophysics, 670, A164
- Purcell, E. M. 1979, ApJ, 231, 404
- Reissl, S., Stutz, A. M., Klessen, R. S., Seifried, D., & Walch, S. 2021, MNRAS, 500, 153
- Reissl, S., Wolf, S., & Brauer, R. 2016, A&A, 593, A87
- Serkowski, K., Mathewson, D. S., & Ford, V. L. 1975, ApJ, 196, 261
- Sugitani, K., Nakamura, F., Shimoikura, T., et al. 2019, PASJ, 71, S7
- Tahani, M. 2022, Frontiers in Astronomy and Space Sciences, 9, 940027
- Tahani, M., Plume, R., Brown, J. C., & Kainulainen, J. 2018, Astronomy & Astrophysics, 614, A100
- Tahani, M., Lupypciw, W., Glover, J., et al. 2022, Astronomy & Astrophysics, 660, A97
- Vaillancourt, J. E., Andersson, B.-G., Clemens, D. P., et al. 2020, ApJ, 905, 0
- Versteeg, M. J. F., Magalhães, A. M., Haverkorn, M., et al. 2023, The Astronomical Journal, 165, 87
- Wang, J.-W., Lai, S.-P., Clemens, D. P., et al. 2020, ApJ, 888, 13
- Whittet, D. C. B. 2003, Dust in the galactic environment
- Whittet, D. C. B., Hough, J. H., Lazarian, A., & Hoang, T. 2008, ApJ, 674, 304
- Zucker, C., Goodman, A., Alves, J., et al. 2021, ApJ, 919, 35